COO-1195-236

A STUDY OF THE DIFFERENTIAL CROSS SECTION OF THE REACTION PI-MINUS PROTON GOES TO OMEGA-ZERO NEUTRON AT 3.65, 4.5 AND 5.5 GeV/c

BY

ALLISON DEAN RUSSELL
S.B., Massachusetts Institute of Technology, 1964
M.S., University of Illinois, 1966

THESIS

Submitted in partial fulfillment of the requirements
for the degree of Doctor of Philosophy in Physics
in the Graduate College of the
University of Illinois at Urbana-Champaign, 1971

Urbana, Illinois

DISCLAIMER

A STUDY OF THE DIFFERENTIAL CROSS SECTION OF THE REACTION PI-MINUS PROTON GOES TO OMEGA-ZERO NEUTRON AT 3.65, 4.5 AND 5.5 GeV/c

BY

ALLISON DEAN RUSSELL
S.B., Massachusetts Institute of Technology, 1964
M.S., University of Illinois, 1966

THESIS

Submitted in partial fulfillment of the requirements
for the degree of Doctor of Philosophy in Physics
in the Graduate College of the
University of Illinois at Urbana-Champaign, 1971

Urbana, Illinois

A STUDY OF THE DIFFERENTIAL CROSS SECTION OF THE REACTION PI-MINUS PROTON GOES TO OMEGA-ZERO OMEGA AT 3.65, 4.5 AND 5.5 GeV/c

Allison Dean Russell, Ph.D.
Department of Physics
University of Illinois at Urbana-Champaign, 1971

A scintillation counter and optical spark chamber experiment has been performed to study the differential cross section for the reaction $\pi^- p \rightarrow \omega^o n$ at 3.65, 4.5 and 5.5 GeV/c. The data show a substantial unnatural parity contribution to the scattering amplitude. The natural parity part of the cross section is not consistent with the predictions of a simple model using Reggeized ρ exchange.

ACKNOWLEDGEMENTS

I wish to express my gratitude to all those who have contributed to this work. Especially, I wish to thank:

Professor Hans Frauenfelder, my advisor, whose guidance, encouragement and enthusiasm for physics have contributed much to my graduate career;

Professor Albert Wattenberg, whose advice during my early work in elementary particle physics was most valuable;

Professors Leland Holloway and David Mortara, without whom this experiment would not have been possible;

my fellow graduate students Eli Rosenberg, Mick Jordan and Larry Nodulman who contributed much hard work and good fellowship;

Dr. Bent Huld; Professors Seymour Bernstein, Donald McLeod and Seymour Marguilies of the University of Illinois at Chicago Circle; and Dr. Martin Garrell for their various contributions to the experiment;

Professor James Smith, Bob Cullum and David Eitelbach, for their efforts programming and maintaining the $\Sigma 2$ computer;

our technicians, Cloyd Smock and Leonard Seward;

Mrs. Mary Jo Pelafas and the scanning and measuring crew;

Mrs. Nancy Czechowski and the 7094 staff; and

Mrs. Estella Thomas.

The expert work by Mrs. Lynn Rowe in preparing this manuscript was most helpful.

Finally, I thank my wife Georgia for her patience and encouragement during these long years of graduate study.

This work was supported by the U. S. Atomic Energy Commission.

TABLE OF CONTENTS

I. INTRODUCTION

An optical spark chamber and scintillation counter experiment has been performed at the Argonne National Laboratory Zero Gradient Synchrotron to study omega meson production in the reaction

$$\begin{array}{l} \pi^- p \to \omega^o n \\ \qquad\quad \hookrightarrow \pi^+\pi^-\pi^o \\ \qquad\qquad\qquad \hookrightarrow \gamma\gamma \end{array} \qquad (I.1)$$

at incident pion momenta of 3.65, 4.5 and 5.5 GeV/c. The differential cross section, $d\sigma/dt$, and the experimentally accessible elements of the spin density matrix of the omega meson, $\rho_{mm'}$, have been measured in the momentum transfer interval $-1.0 \leq t \leq -.05$ $(GeV/c)^2$ at each of the three beam momenta.

Reaction (I.1) is very appealing for analysis in terms of peripheral (especially, Regge) models. Isospin and G-parity conservation restrict the quantum numbers which can be exchanged in the t-channel for this reaction to $I^G = 1^+$. Of the known low-lying meson states, only the $\rho(765)$ with $J^P = 1^-$ and the B(1235) with $J^P = 1^+$ have the proper quantum numbers.[1] In terms of Regge models, only one natural parity trajectory, the ρ, and one unnatural parity trajectory, the B, may be exchanged.

It is well known that for vector meson production in reactions of the type P + B → V + B, the helicity zero state of the vector meson can only be populated by an unnatural parity t-channel exchange.[2] It has also been shown by Ader, et al.,[3] that appropriate linear combinations of the spin density matrix elements of the vector meson isolate the natural and unnatural parity contributions to the scattering amplitude. In omega production only one exchange of each type is allowed, and a particularly clean separation of these effects may be expected.

In this experiment the π^- beam was incident on a liquid hydrogen target surrounded on five sides by scintillation counters to veto events which produced charged particles at wide angles. The vector meson decay products were detected in the forward direction in a counter hodoscope and thin foil and heavy plate spark chambers. The counter hodoscope required two charged particles in the forward direction for a valid trigger. The thin foil spark chambers were used to determine the directions of the charged particles. Conversion of the gammas in the heavy plate chambers was an essential part of the event selection criteria. Recoil neutrons were detected in a counter hodoscope which determined both their direction and time of flight.

In Chapter II the theoretical background is reviewed briefly. In Chapter III details of the data collection procedure and the apparatus are presented. Data reduction and analysis methods are discussed in Chapter IV. Results and conclusions are presented in Chapter V.

II. THEORETICAL BACKGROUND

Peripheral and Regge models provide the framework within which most two-body and quasi-two-body interactions at energies above a few GeV are analyzed.[4-6] We will consider here only simple Regge pole models for the reaction

$$\pi^- p \rightarrow \omega n \qquad (II.1)$$

and the general features they require of the data.

Peripheralism instructs us to try to understand reaction (II.1) in terms of the single particle, or Reggeon, exchange (Figure II.1). In the corresponding t-channel reaction

$$p\bar{n} \rightarrow \pi^+ \omega \qquad (II.2)$$

isospin and G-parity conservation at the $\pi^+\omega$ vertex require the exchanged particle to have $I^G = 1^+$. Among the known low-lying meson resonances only the $\rho(765)$ with $J^P = 1^-$ and the $B(1235)$ with $J^P = 1^+$ have the appropriate quantum numbers.[1]

The usual Regge assumption is that at sufficiently high energies the scattering amplitude is dominated by the highest-lying trajectory. Wang[7] has used this to predict the existance of a dip in the differential cross section at $t \sim -0.6\ (\text{GeV}/c)^2$. This dip is caused by the vanishing of the helicity-flip amplitude[8] where the ρ-trajectory passes through zero. This prediction is in complete disagreement with experiment. Several other authors[9-11] constructed models based on both ρ and B exchange which gave satisfactory fits to the data.

Figure II.1. One particle exchange diagram for $\pi^- p \rightarrow \omega n$.

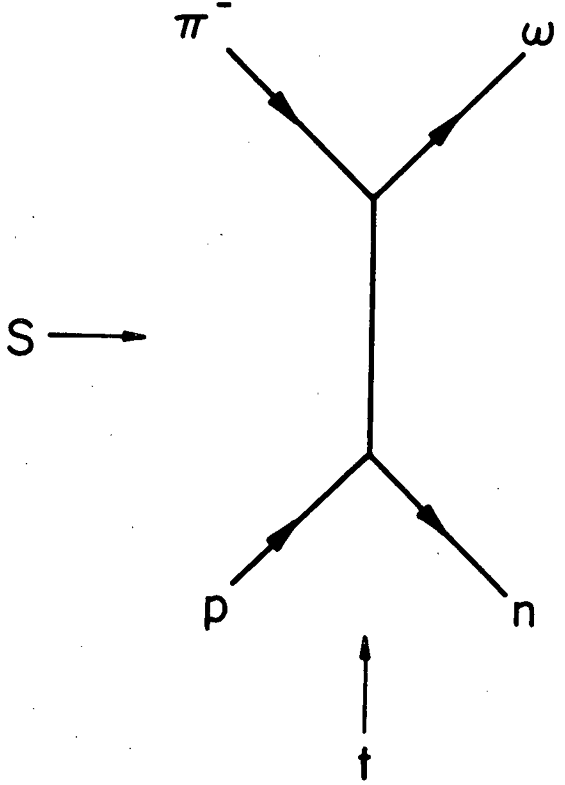
π^-
ω
S
p
n
t

To extract the essential qualitative features of these models for comparison with experiment it is necessary to examine the spin density matrix of the omega meson. Gottfried and Jackson[2/] have shown that exchange of a natural parity object (the ρ) cannot populate the helicity 0 state of the vector meson. Thus, the spin density matrix elements ρ_{00} and ρ_{10} provide a direct measure of the contribution of unnatural parity exchanges to the amplitude for reaction (II.1). Ader, et al.[3/] have shown further that $\rho_{11} + \rho_{1-1}$ $(\rho_{11}-\rho_{1-1})$ isolates the natural (unnatural) parity contribution to the production amplitude. Thus

$$\frac{d\sigma_n}{dt} = (\rho_{11}+\rho_{1-1}) \frac{d\sigma}{dt} \sim F_1(t)\left(\frac{s}{s_o}\right)^{2\alpha_\rho(t)-2} \tag{II.3a}$$

$$\frac{d\sigma_u}{dt} = [\rho_{00} + (\rho_{11}-\rho_{1-1})] \frac{d\sigma}{dt} \sim F_2(t)\left(\frac{s}{s_o}\right)^{2\alpha_B(t)-2} \tag{II.3b}$$

provide explicitly predictions about the energy dependences of the two parts of the differential cross section. The ratio of natural to unnatural parity parts is

$$R = \frac{\rho_{11} + \rho_{1-1}}{\rho_{00} + (\rho_{11}-\rho_{1-1})} = F_3(t)\left(\frac{s}{s_o}\right)^{2(\alpha_\rho(t)-\alpha_B(t))} \tag{II.4}$$

and a plot of ln R versus ln s should be a straight line with slope $2(\alpha_\rho(t)-\alpha_B(t))$.

From the form

$$\frac{d\sigma}{dt} = F(t)\ s^{2\alpha(t)-2} \tag{II.5}$$

and the assumption

$$\alpha(t) = \alpha(0) + \alpha' t \tag{II.6}$$

one obtains

$$\sigma \sim s^{2\alpha(0)} \int_{-\infty}^{0} F(t)\, e^{2\alpha' t \ln s}\, dt \ . \qquad \text{(II.7)}$$

The integral may be expected to have only a logarithmic dependence on s and the dominant energy dependence of the cross section is then given by

$$\sigma \sim s^{2\alpha(0)-2} \ . \qquad \text{(II.8)}$$

Equation (II.3) and (II.8) may be used to examine the t=0 intercepts of the ρ and B trajectories. In general, when more than one trajectory is expected to contribute to $d\sigma/dt$, (II.8) should give an effective intercept, α_{eff}, reflecting the combined effects of these trajectories.

A detailed discussion of the properties of the spin density matrix of the omega meson has been given by Rosenberg.[12]

III. EXPERIMENTAL METHOD I: DATA COLLECTION

The experimental apparatus was arranged to trigger selectively on events characteristic of reaction (I.1) in the momentum transfer interval $-1.(\mathrm{GeV}/c)^2 \leq t \leq -.05(\mathrm{GeV}/c)^2$. A valid trigger required an incident π^- beam particle to interact in the liquid hydrogen target, a recoil neutron to be detected in an appropriate time-of-flight interval and two charged particles to be detected in a counter hodoscope downstream of the target. A charged particle in the beam line downstream of the target or at an angle too large to be consistent with ω production provided a veto signal.

For valid events, optical spark chambers were used to record directional information for the charged tracks and showers produced by the gammas from the π^0 decay. The chambers were photographed in 90° stereo.

A. The Beam

The experiment was performed in beam No. 17 at the Argonne National Laboratory Zero Gradient Synchrotron (the 17° beam). This is an unseparated π^- beam produced by targetting the circulating beam internally. Negative particles were channeled down the 17° beam line by three quadrupole magnet doublets and two bending magnets as shown in Figure III.1. The freon-filled Cherenkov counter was used as a threshold counter to veto muons and electrons.

The momentum-defining slit was immediately upstream of the freon Cherenkov counter. This slit also controlled the beam intensity. At the highest intensity used, the momentum spread was ± 1%; for most of the data, ± 0.75%.

Figure III.1. Beam transport system. Experimental layout, including neutron counters, is shown in upper left corner.

BEAM TRANSPORT SYSTEM
ARGONNE ZGS EXPERIMENT E-201

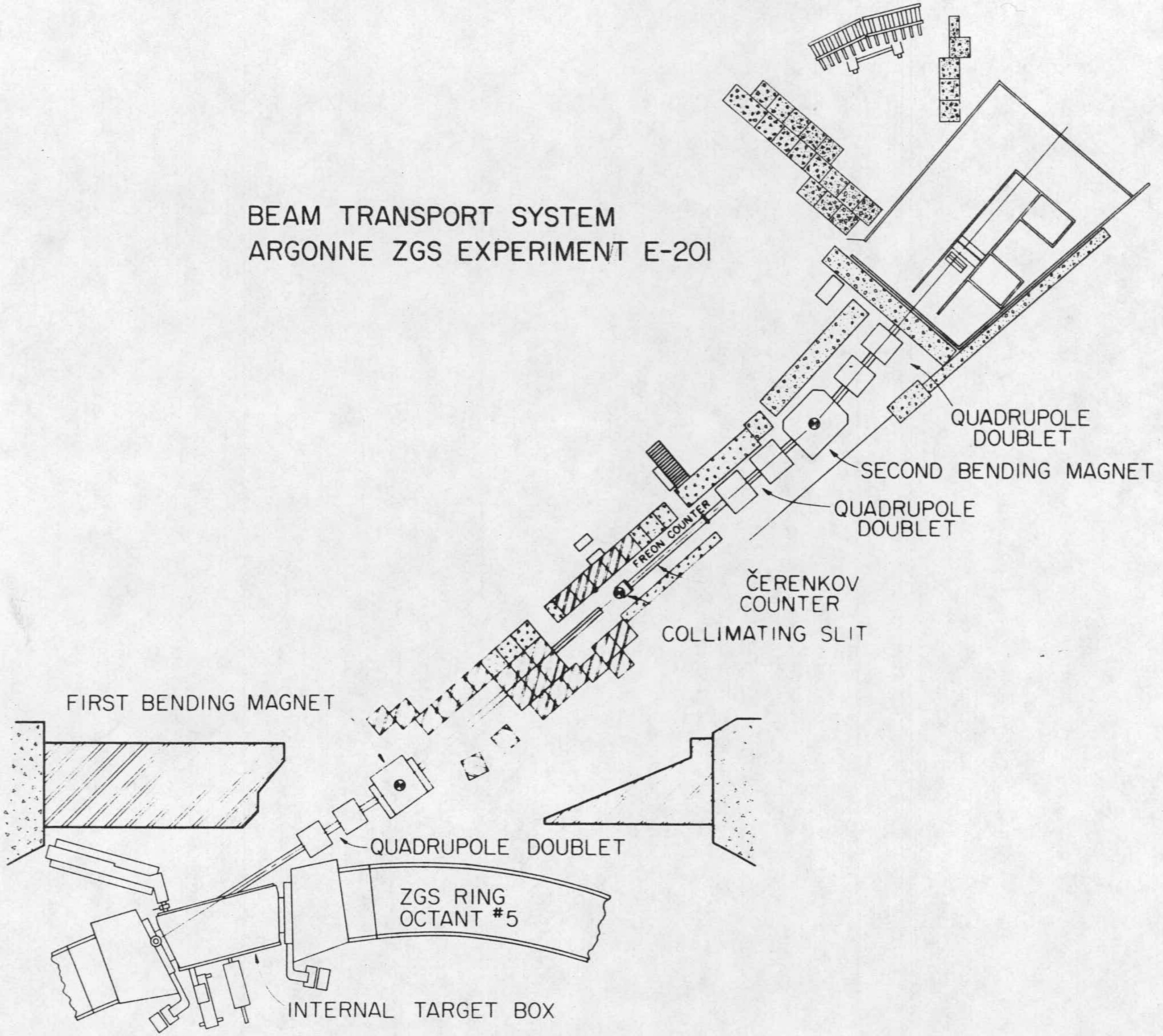

In separate runs, the beam transport system was adjusted to pass particles with momenta of 3.65, 4.5 or 5.5 GeV/c. Count rates in the beam telescope, B_o B_1 B_2 (see Figure II.2) were maintained between 100,000 and 200,000 particles per pulse. The beam pulse had a 450-600 millisecond flat-top and the Z.G.S. repetition rate was approximately one pulse every 3.6 seconds.

The final focus of the beam was between counters B_2 and B_3 (Figure III.2). The resulting beam-spot size at the upstream end of the liquid hydrogen target was 3.2 cm horizontally and 1.3 cm vertically. The half-angle beam divergences were 7 milliradians horizontally and 10 milliradians vertically.

B. Liquid Hydrogen Target

The liquid hydrogen target was constructed and maintained by the A.N.L. Liquid Hydrogen Target Group. It was the closed system (recirculating) type, cooled by a 10 watt capacity helium refrigerator mounted above the target flask. The target flask was a cylinder 30 cm long and 5 cm diameter with a capacity of approximately 0.6ℓ.

C. Experimental Layout

The experimental layout is shown schematically in Figure III.2. Counters B_o, B_1, B_2 and HA formed the beam defining telescope. B_1 also provided the start signal for the measurement of the neutron's time-of-flight. Counter BA vetoed events with a charged track in the beam line downstream of the target.

Figure III.2. Experimental layout.

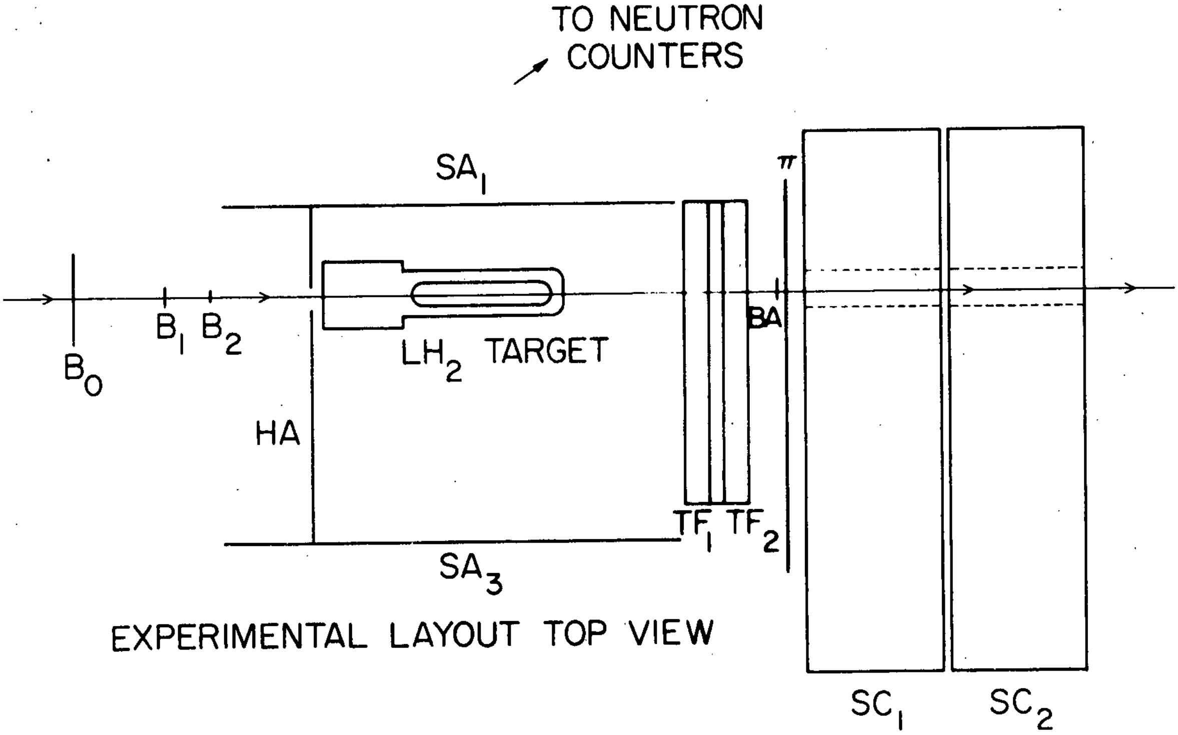

EXPERIMENTAL LAYOUT TOP VIEW

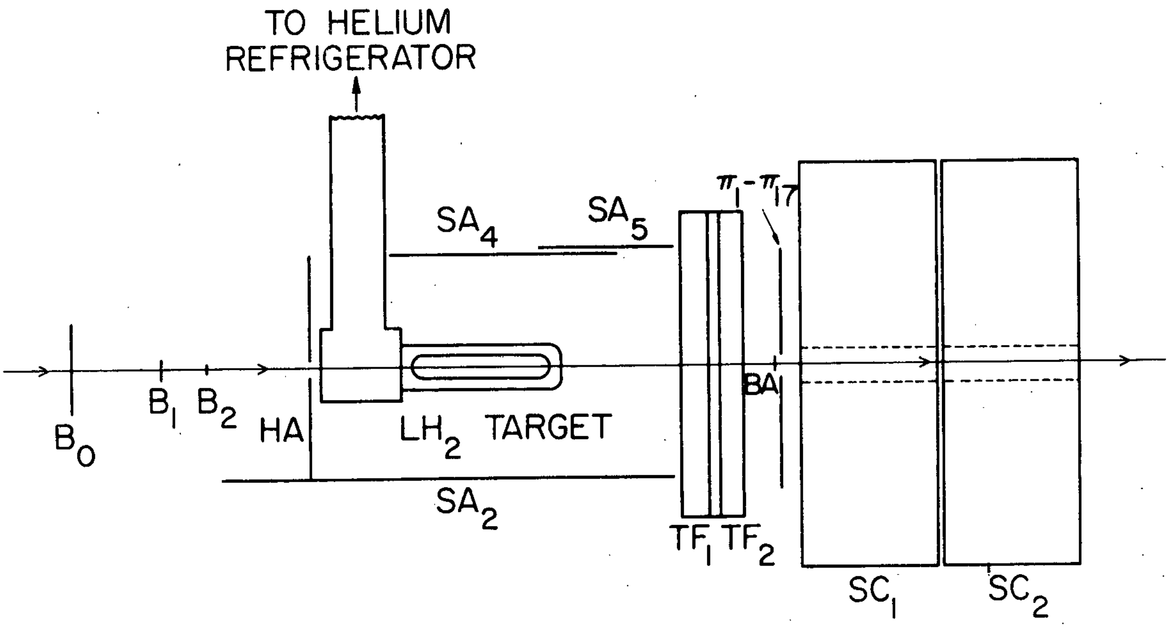

EXPERIMENTAL LAYOUT SIDE VIEW

Anti-counters SA_1-SA_5 and HA formed a box surrounding the target on five sides to veto any interaction producing a charged secondary at large angles. Five additional anti-counters, WA_1-WA_5 (not shown), were arranged to veto on charged particles emerging in the forward direction, but at angles too large to be consistent with omega production.

Counters π_1-π_{17} (the π-hodoscope) were arranged in a horizontal array to detect forward-going charged particles. We demanded that 2 and only 2 π-counters fire as part of a valid event signature.

The 52 neutron counters (not shown in Figure III.2) were arranged in a 4 x 13 matrix (Figure III.3) along a circle of approximately 10 m radius centered on the target. In the horizontal direction, the counters were separated by approximately two counter widths. (The counters were 10 cm wide by 25 cm high by 30 cm deep.) During data taking, successive runs were made with the array alternately in one of three positions differing by one counter width to provide uniform coverage of the angular interval.

Details of the counter dimensions, materials and phototubes are given in the thesis by Rosenberg.[12/]

The four spark chambers are labelled TF_1, TF_2, SC_1 and SC_2 in Figure III.2. TF_1 and TF_2 were constructed using thin aluminum foil plates. Each one had 4 gaps, 1 cm wide and an active area 69 cm by 69 cm. They were used to determine the direction of the two required charged tracks.

The shower chambers, SC_1 and SC_2, served a dual purpose, providing additional data on the directions of the charged tracks and determining the points of conversion of the gamma rays. Each chamber had 20 gaps

Figure III.3. Neutron counter matrix as seen from target.

NEUTRON COUNTERS AS SEEN FROM TARGET

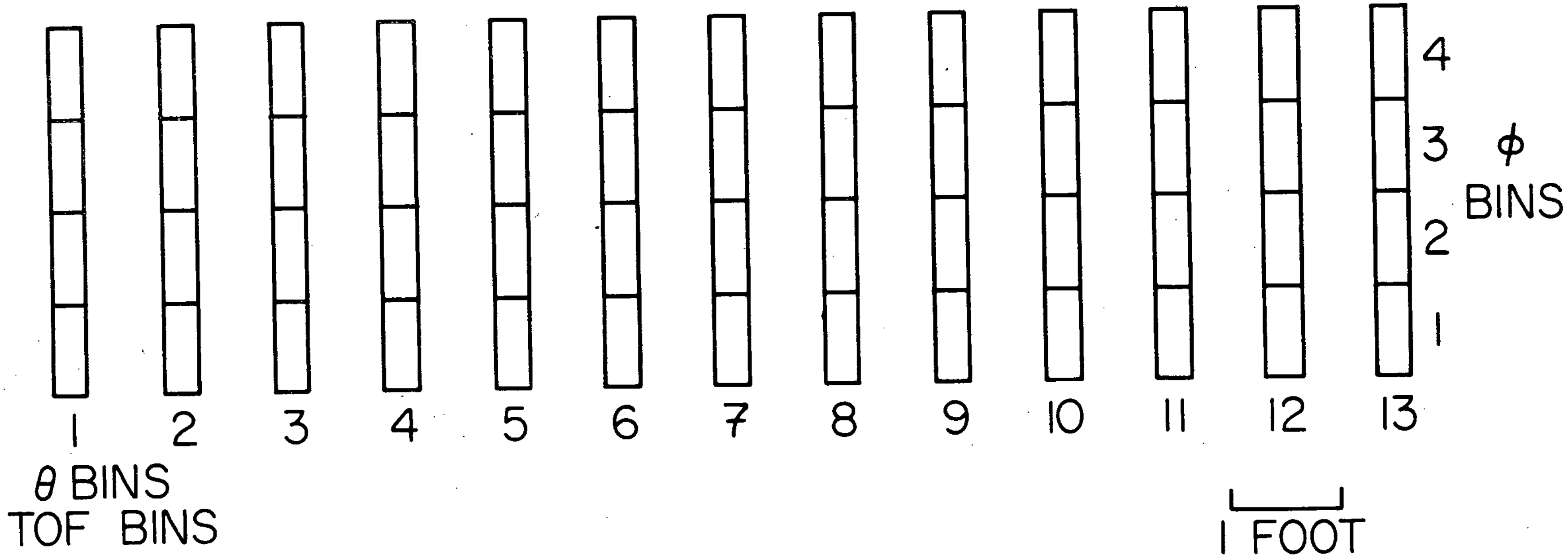

1 cm wide and an active area 91 cm by 122 cm. To give useful data on the directions of the charged tracks, the first seven plates in SC_1 were aluminum, 0.31 cm thick. To provide a high gamma conversion probability, the following 14 plates in SC_1 and all 21 plates in SC_2 were an aluminum-lead-aluminum sandwich, 0.76 mm Al -- 1.52 mm Pb -- 0.76 mm Al. The 35 Al-Pb-Al plates placed ~ 9.5 radiation lengths of material in the photons' flight paths.

To minimize beam particle interactions in the spark chambers, there was a 7.6 cm diameter hole through SC_1 and SC_2 along the beam line.

D. Logic

The neutron counter logic is shown in Figure III.4; the time-of-flight and trigger logic, in Figure III.5. The electronics was a combination of EG&G, University of Illinois and Lecroy Research Systems fast logic modules.

Four 50 ohm signals were available from each neutron counter, 2 from the anode and 1 each from the 13th and 14th dynodes.* These signals were used to determine the neutron's scattering angle, θ, its time-of-flight (TOF), the azimuthal angle, ϕ, of the scattering plane and the pulse height. Within each column of 4 counters one set of anode signals was passively added to provide 13 TOF signals; similarly, the (inverted) outputs from the 14th dynodes provided 13 θ signals. Along each row of 13 counters, the remaining anode outputs were passively added to yield 4 ϕ signals. The remaining 52 outputs (from the 13th dynodes) were

---

*The 58AVP phototube used on the neutron counters is a 14 stage device.

NEUTRON COUNTER LOGIC (PULSE HEIGHT LOGIC NOT SHOWN)

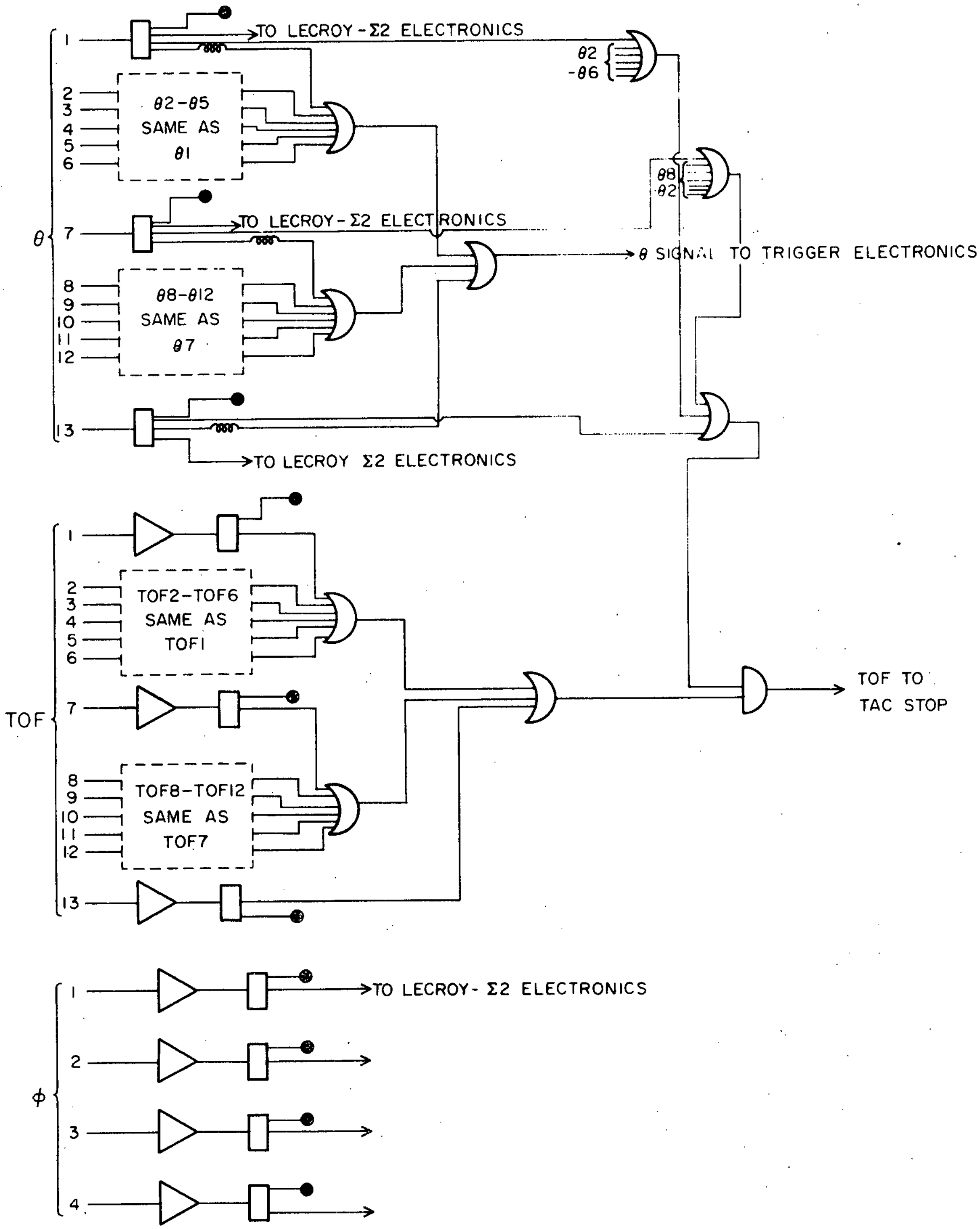

Figure III.5. Time-of-flight and trigger logic.

TRIGGER AND TIME OF FLIGHT LOGIC DIAGRAM

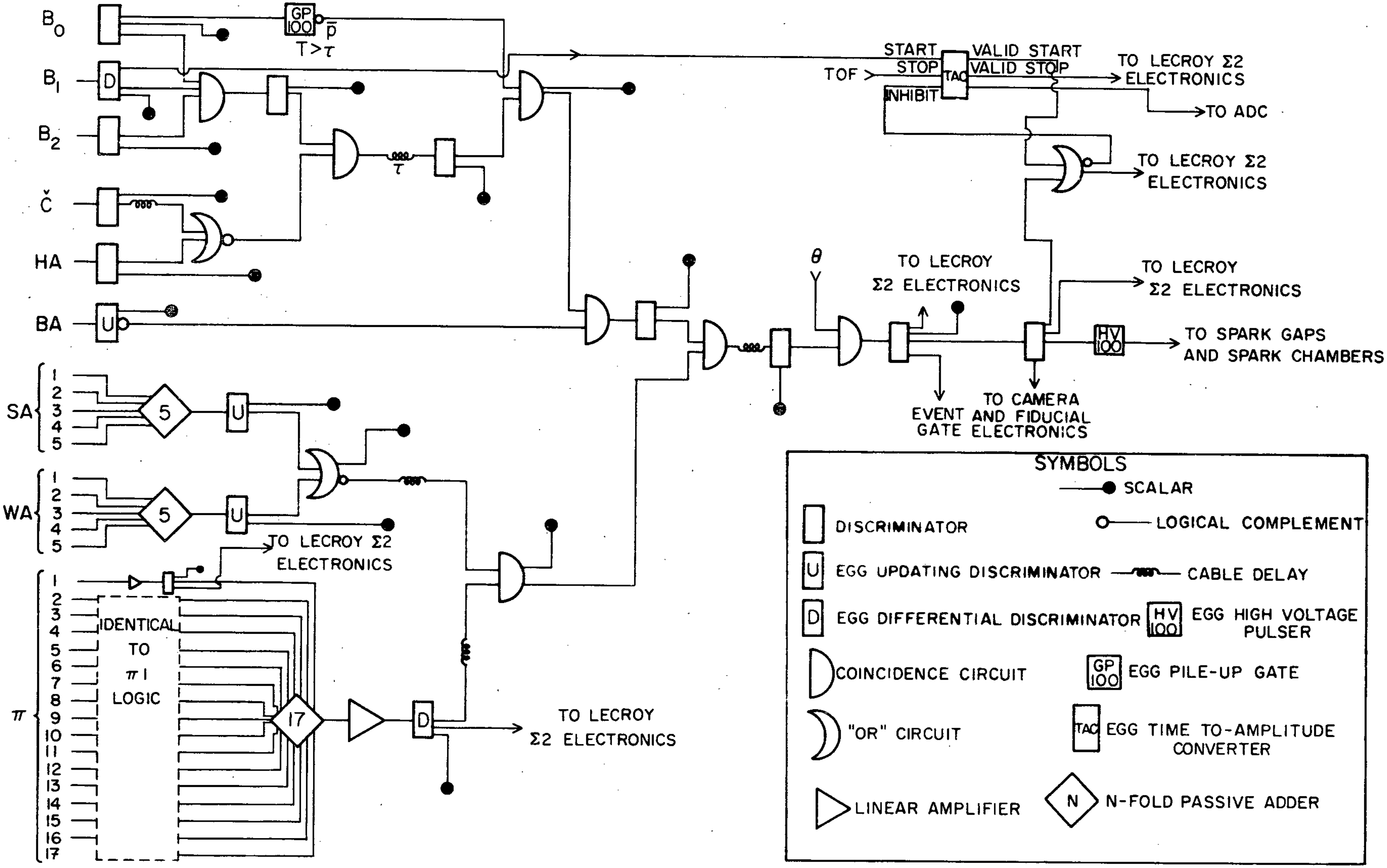

passively added to give the pulse height information. The pulse height was recorded by a Lecroy 8-bit analog-to-digital converter (ADC). The pulse height logic is not shown.

The 13 TOF signals drove 13 discriminators, set with very low threshold (~ 1 MeV energy loss in the counter). The 13 θ signals also drove 13 discriminators, but with a much higher threshold setting (~ 6 MeV energy loss). The output signal from the θ discriminators was much wider than that from the TOF discriminators (20 ns and 5 ns respectively) and the TOF signal was approximately centered on the θ signal. A coincidence between θ and TOF then caused the timing information to be defined by the TOF signal. This high-low discrimination technique was used to minimize the effect of slewing on the time-of-flight measurement and at the same time to discriminate effectively against the low energy neutron background at the Z.G.S.

An EG&G time-to-amplitude converter (TAC) was used for the time-of-flight measurement. The START signal to the TAC was provided by B_1. The gated TOF signal triggered the TAC STOP. A Lecroy ADC converted the TAC output to digital form.

To select events with two charged particles in the π-hodoscope, the outputs from the 17 π-counter discriminators were passively added and the 2π signal was generated by using an EG&G differential discriminator to require that 2 and only 2 π-counters fired.

A valid trigger was defined electronically by

$$(B_o\ B_1\ B_2)(2\pi)(\theta)\ \overline{\check{C}}\ \overline{BA}\ \overline{HA}\ \overline{SA}\ \overline{WA}$$

Such a signature initiated the following sequence of events: The spark chambers were fired, certain indicative information was displayed on binary coded lights for photographic recording and also placed on the Lecroy data bus, and the camera was advanced. The indicative information consisted of run number, event (frame) number, neutron time-of-flight, neutron counter pulse height and θ- and ϕ-indices for the neutron counter that fired. Multiple θ or ϕ hits were allowed, but were flagged. In addition, the numbers of the π-counters which fired were also transmitted on the data bus, but were not recorded photographically. The data on the Lecroy bus were transmitted to the on-line XDS $\Sigma 2$ computer. A Kennedy incremental tape recorder was also available and used as a back-up for, or in addition to, the computer.

E. The On-Line Computer

The on-line XDS $\Sigma 2$ computer preformed several functions: to buffer the transmission of the indicative information from data bus to magnetic tape, to perform preliminary calculations on these data, to write these results together with the indicative information on magnetic tape, and to accumulate a variety of histograms used to monitor the progress of the experiment.

The high data-taking rate of the computer was used to monitor the calibration of the time-of-flight electronics. During normal operation the data rate was limited by the camera recycle time. About once every six runs, the camera and spark chambers were disabled, the timing gates of the neutron counters were changed and a high statistics run was made, detecting the gammas from events of the type

$$\pi^- + p \rightarrow \gamma + \text{anything}$$

in the neutron hodoscope. These "prompt peaks" were used to define the zero for the time-of-flight scale.

The ability of the computer to perform simple calculations, in real time, for each event made possible the operation of the experiment as a missing-mass spectrometer. The neutrons' energy and momentum were calculated from the neutron's time-of-flight and direction (defined by the θ signal). The missing-mass was then obtained from

$$(MM)^2 = m_\pi^{\ 2} + (m_n - m_p)^2 - 2E_\pi(m_n - m_p) - 2(m_p + E_\pi)T_n + 2p_\pi p_n \cos\theta \qquad \text{(III.1)}$$

in terms of laboratory quantities. In the on-line calculations, terms proportional to $(m_n - m_p)$ were neglected. On-line resolution of the missing-mass spectrometer was limited by three factors: it was necessary to assume the interaction vertex was at the center of the target, and thus to accept a large uncertainty in the scattering angle, θ; the path lengths for the neutron time-of-flight measurements were not well known; and the timing information on the prompt peaks was not up-dated after the initial calibration. Mass spectra calculated later using correct prompt peak and counter position data are shown in Figure III.6. The histograms accumulated on line were similar except for slightly poorer resolution.

F. Time-of-Flight Measurement

The time-of-flight (TOF) was calculated from

$$\text{TOF} = \frac{d}{c} + \delta + S(T_{ADC} - T_{ADC}^{\text{prompt}}). \qquad \text{(III.2)}$$

Figure III.6. Missing-mass spectra calculated using prompt peak and counter position data.

SPECTROMETER MASS DISTRIBUTIONS AT 4.5 GeV/c

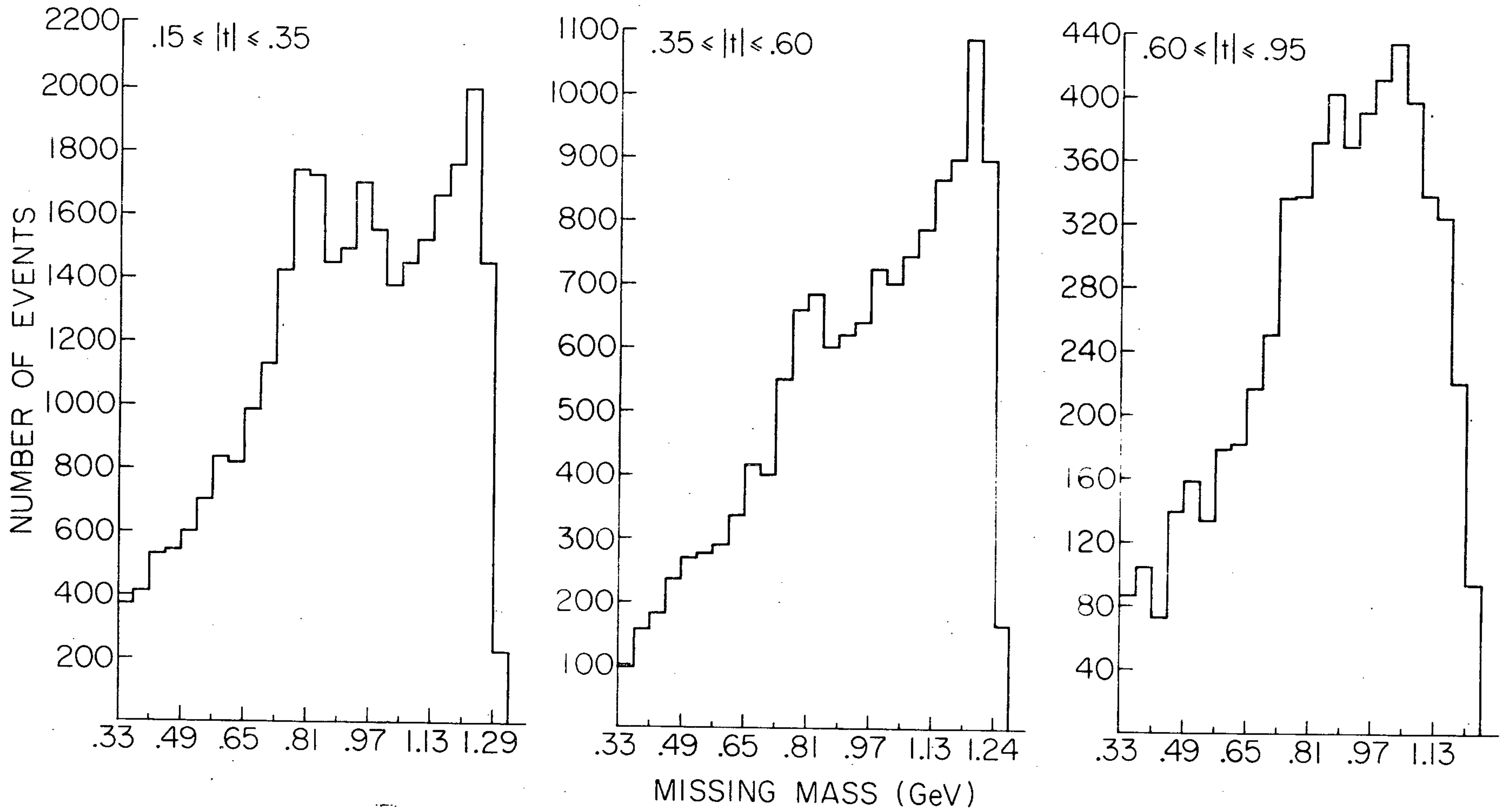

In this expression, d is the length of the neutron's flight path, T_{ADC} (T_{ADC}^{prompt}) is the ADC channel for the event (prompt peak in the appropriate counter), and S is a scale factor equal to 0.53 ns per channel. The quantity δ is discussed below.

In the analysis of fitted events, the distance d was computed for each event from the reconstructed vertex to the center of the appropriate neutron counter. For the on-line processing, d was taken as constant, d=10 m.

During normal operation, the delays and gates in the TOF electronics were adjusted so that the situation illustrated in Figure III.7(a) was obtained, and the prompt peak (γ's from $\pi^- p \rightarrow \gamma$ + anything) was outside the TAC-ADC range. During the prompt peak runs, the timing was changed (Figure III.7(b)), moving the prompt peak by δ and bringing it into the TAC-ADC range. All other measurements are then referred to this prompt peak position.

The resolution of the TOF electronics was checked in two ways: by looking at the width of the prompt peak spectrum and by looking at the coincidence resulting from ^{60}Co decay. The two checks were consistent, and the resolution was taken to be ± 1 ns.

Figure III.7. Schematic illustration of timing difference between normal and prompt peak runs.

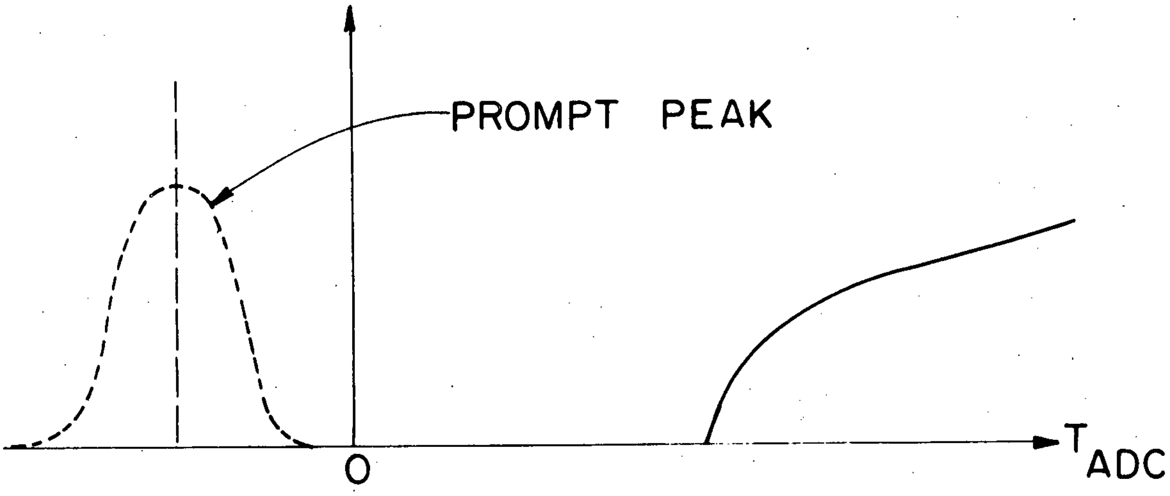

(a) NORMAL OPERATION

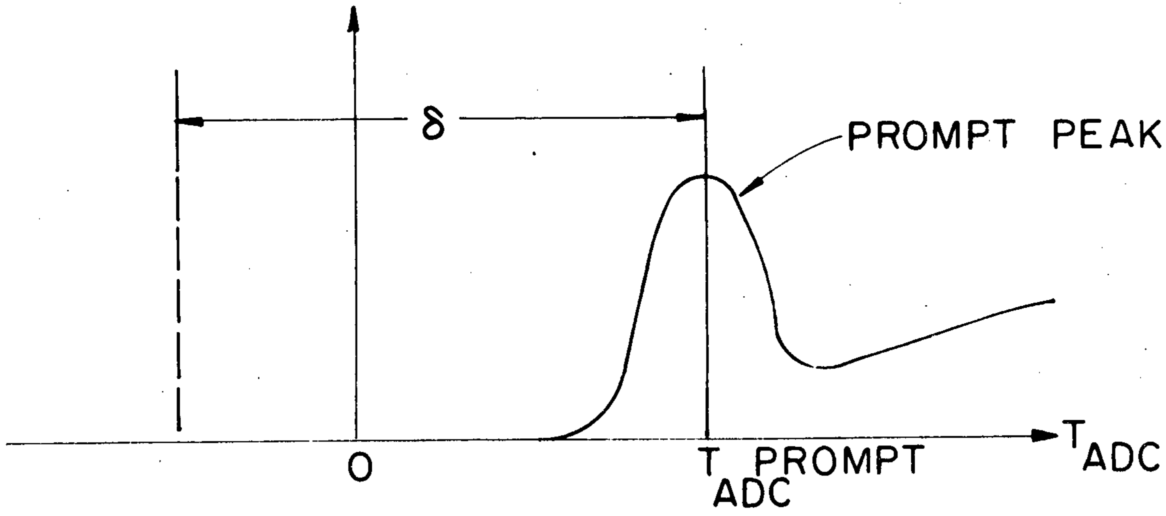

(b) ILLUSTRATING TIMING MODIFICATION FOR PROMPT PEAK RUNS

IV. EXPERIMENTAL METHOD II: DATA REDUCTION

A. Pre-scanning Event Selection

During data collection, the range of missing mass accepted was kinematically constrained. A typical family of curves is given in Figure IV.1, showing the relation between time-of-flight and neutron laboratory angle for a series of missing masses. The cross hatched region shows the constraints placed on the missing mass by the timing gates.

The raw data were subjected to further cutting on the basis of the spectrometer missing-mass in the preparation of scan lists. In its simplest form, this cut simply excluded all events for which $(MM)^2 \leq 0$ in equation (III.1).

Another, more sophisticated, cut was developed and applied to the remaining data. For each event, an ellipse was constructed in the θ-TOF plane with semi-axes of approximately 4 standard deviations in each direction (76 mr in θ and 6 ns in TOF respectively). Those events for which the omega mass curve passed through this ellipse were accepted for scanning. In addition, all events with a spectrometer mass in the range $0.54\ \mathrm{GeV}/c^2 \leq MM \leq 1.03\ \mathrm{GeV}/c^2$ were accepted. This cut eliminated approximately 50% of the events.

To check the validity of this cut, a sample of the data was processed using both cuts and a corrected spectrometer mass was calculated. No events with a corrected mass in the range $0.56\ \mathrm{GeV}/c^2 \leq MM \leq 1.0\ \mathrm{GeV}/c^2$ were removed by the (stronger) second cut.

Figure IV.1. Neutron time-of-flight versus laboratory angle for a series of missing masses. The acceptance limits defined by the timing gates are outlined.

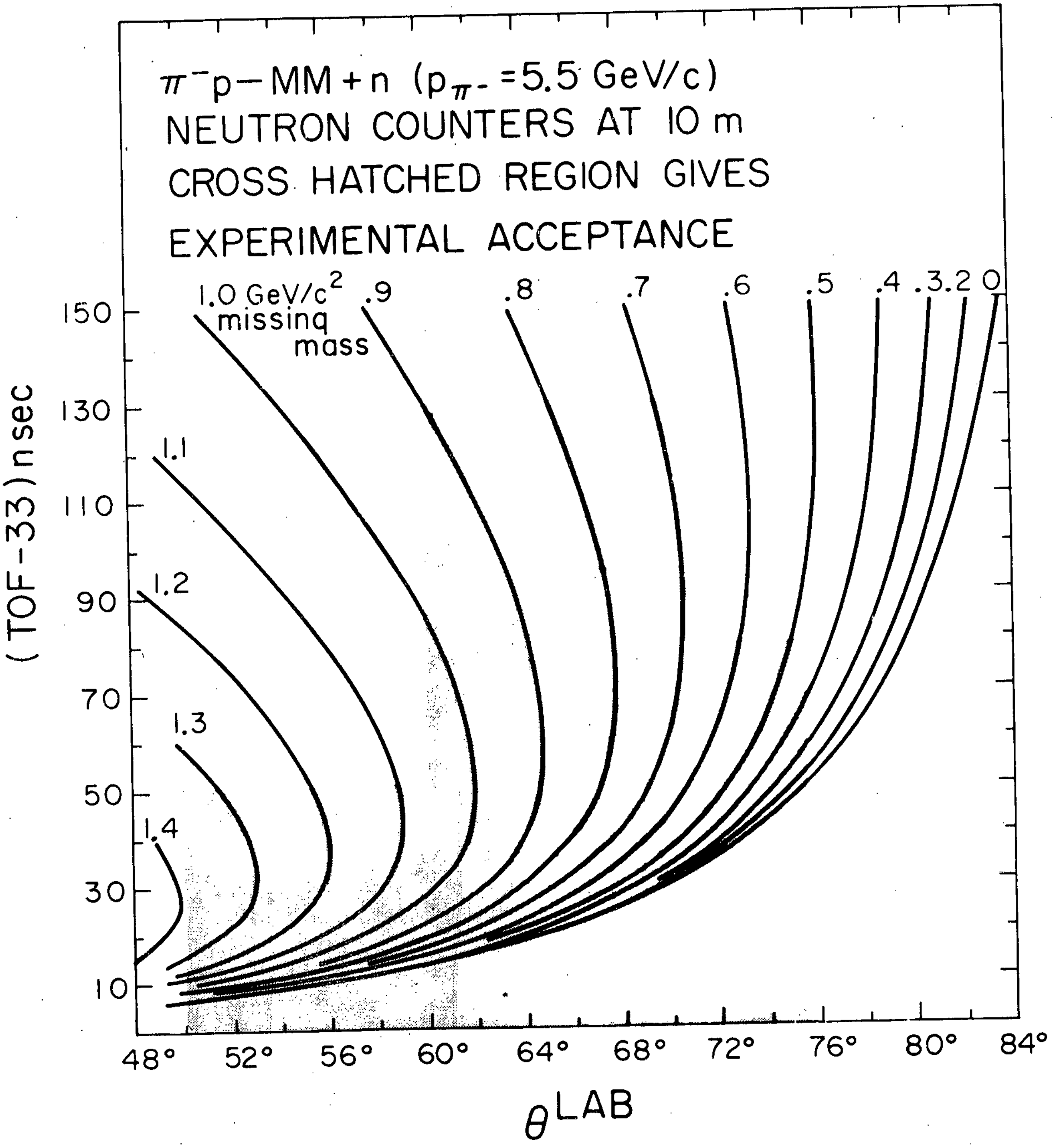
$\pi^- p \rightarrow MM + n$ (p_{π^-} =5.5 GeV/c)
NEUTRON COUNTERS AT 10 m
CROSS HATCHED REGION GIVES
EXPERIMENTAL ACCEPTANCE
1.0 GeV/c^2 missing mass
.9
.8
.7
.6
.5
.4
.3
.2
0
1.1
1.2
1.3
1.4
(TOF-33) nsec
150
130
110
90
70
50
30
10
48°
52°
56°
60°
64°
68°
72°
76°
80°
84°
θ^{LAB}

B. Scanning and Measuring

Scanning personnel were instructed to separate events into five categories: (i) chamber breakdown; (ii) zero-shower events; (iii) one-shower events; (iv) two-shower events; and (v) more-than-two-shower events.

For scanning purposes, a shower was defined as five or more associated sparks, visible in both views, not associated with an interaction of another particle upstream of the shower but in the spark chambers, and having no sparks in the foil chambers. Additional criteria allowed the scanners to distinguish charged tracks which were not visible in the foil chambers from showers.

A portion of the film was scanned a second time and conflicts between the two scans were resolved. From these results, it is estimated that the single scan efficiency for detecting two shower events was 70% to 75% or less.

Events selected by the scanners as two shower candidates were then submitted for measuring. The measurers rejected events that were improperly classified by the scanners, events for which the interaction vertex was obviously not in the liquid hydrogen target and events whose image plane topology made measurement impossible.

Accepted two-shower events were measured on a University of Illinois scanning and measuring projector (SMP). The measurement digitized the reprojected image plane positions of a set of four fiducial crosses, the top and side view coordinates of the sparks defining the two charged particle paths, and the top and side view coordinates of the first spark in each shower.

A detailed summary of the scanning and measuring results is given in APPENDIX A.

C. Geometric Reconstruction and Kinematic Fitting

The measured two-shower events were reconstructed in space using a least-squares fitting routine. The optical constants necessary to effect the transformation from film plane to laboratory coordinates were determined from a set of 120 fiducial marks which were fixed to the spark chambers and surveyed relative to the laboratory coordinates. Four fast fiducial crosses (electroluminescent panels) were photographed with each event and, every hundred frames, with the full set of 120 cross-hairs. The optical constants describing the transformation from the SMP image plane to the film plane were independently monitored biweekly during the measuring period.

The SMP image-plane coordinates of the measured points were transformed to space coordinates. A least-squares fit was then attempted to determine the event vertex from the intersection of the two charged tracks. The directions of the gammas were obtained from the fitted vertex and the measured positions of the lead sparks. The vertex and the neutron counter that fired determined the neutron's direction. The quantities supplied by this program were the direction cosines of all five final state particles and the three coordinates, with errors, of the vertex.

The results from the geometric reconstruction and the neutron time-of-flight, calculated using equation (III.2), were used as input to another least-squares fitting program. This program attempted a kinematic fit to the 1 constraint hypothesis

$$\pi^- p \to \pi^+ \pi^- \pi^o n \quad . \tag{IV.1}$$

The effect of the kinematic fitting procedure on the signal-to-noise ratio is shown in Figure IV.2 where the mass spectra (at 4.5 GeV/c) of events submitted for measuring as two-shower events of the final data sample are plotted. The results at 3.65 GeV/c and 5.5 GeV/c are comparable.

A study of the efficiency of the kinematic fitting program was made using a sample of Monte Carlo generated omega events, suitably modified to correspond to known measurement errors. Approximately 10% either failed to fit or were rejected after fitting. Of a sample of randomly distributed background events, approximately 5% gave a satisfactory kinematic fit.

A series of cuts on the results of the kinematic fitting produced the final data sample. These cuts required the fitted event to have a $\chi^2 \leq 16$, an energy imbalance of less than 5 MeV between initial and final states, both photon energies greater than 80 MeV and to satisfy a set of geometric conditions. For each t interval, appropriate omega and control mass regions were defined. The final data sample, after background subtraction, contained 567 omega events at 3.65 GeV/c, 562 at 4.5 GeV/c and 395 at 5.5 GeV/c.

The decay amplitude for a 1^- particle into 3 pions may be written

$$M \sim \vec{\varepsilon} \cdot (\vec{p}_{\pi+} \times \vec{p}_{\pi-}) \tag{IV.2}$$

and the resultant Dalitz plot density,

Figure IV.2. Mass spectra showing the improvement in signal-to-noise ratio due to kinematic fitting.

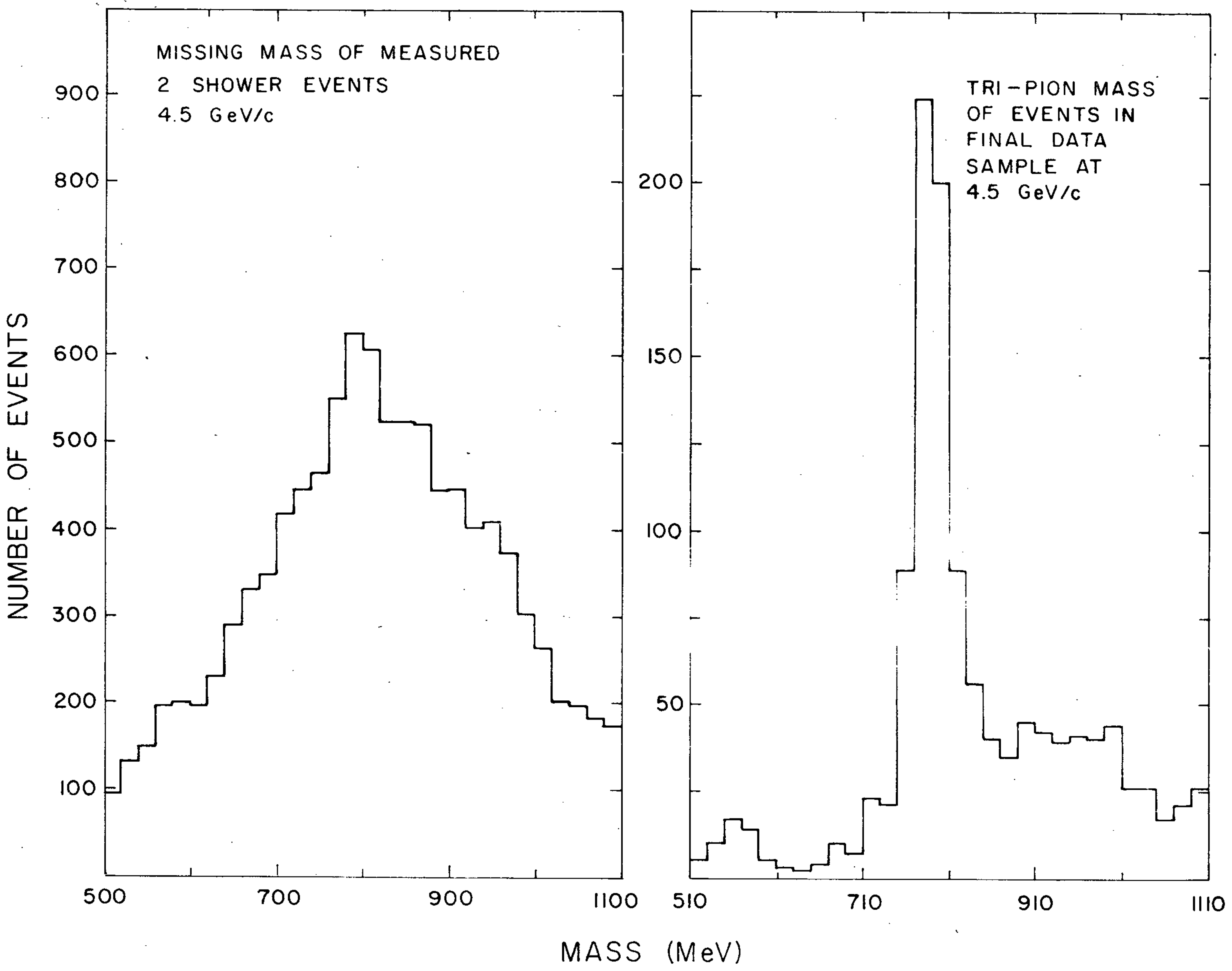
MISSING MASS OF MEASURED
2 SHOWER EVENTS
4.5 GeV/c
TRI-PION MASS
OF EVENTS IN
FINAL DATA
SAMPLE AT
4.5 GeV/c
NUMBER OF EVENTS
900
800
700
600
500
400
300
200
100
200
150
100
50
500
700
900
1100
510
710
910
1110
MASS (MeV)

$$D \sim |\vec{p}_{\pi+} \times \vec{p}_{\pi-}|^2 . \qquad \text{(IV.3)}$$

In Figure IV.3 the number of events is plotted versus

$$\delta = |\vec{p}_{\pi+} \times \vec{p}_{\pi-}|^2 \,/\, |\vec{p}_{\pi+} \times \vec{p}_{\pi-}|^2_{max} \qquad \text{(IV.4)}$$

after the background subtraction. The results are in good agreement with the expected straight line distribution. The events in the control region do not show this behavior. We conclude that the subtracted distributions represent relatively pure omega samples.

Monte Carlo studies showed that vertices of omega events should be uniformly distributed along the beam. The distributions for omega events are shown in Figure IV.4; those for all reconstructed events, in Figure IV.5. The peaking toward the downstream end of the target seen in the sample of all reconstructed events is not present in the final sample, supporting the conclusion that the background subtraction is correct.

D. Experimental Biases

The experimental biases in detection efficiency may be conveniently divided into two classes: those that exhibit a strong dependence on momentum transfer but are independent of the decay angles in the Gottfried-Jackson frame;[2/] and those that depend strongly on the decay angles but are essentially independent of momentum transfer. The density matrix elements are not affected by the t-dependent biases; both the differential cross sections and the density matrix elements are influenced by the biases dependent on the decay angles.

Figure IV.3. Radial Dalitz plot distributions. The vertical scale is in arbitrary units.

RADIAL DALITZ PLOT DISTRIBUTIONS
ω MASS REGION (AFTER BACKGROUND SUBTRACTION)

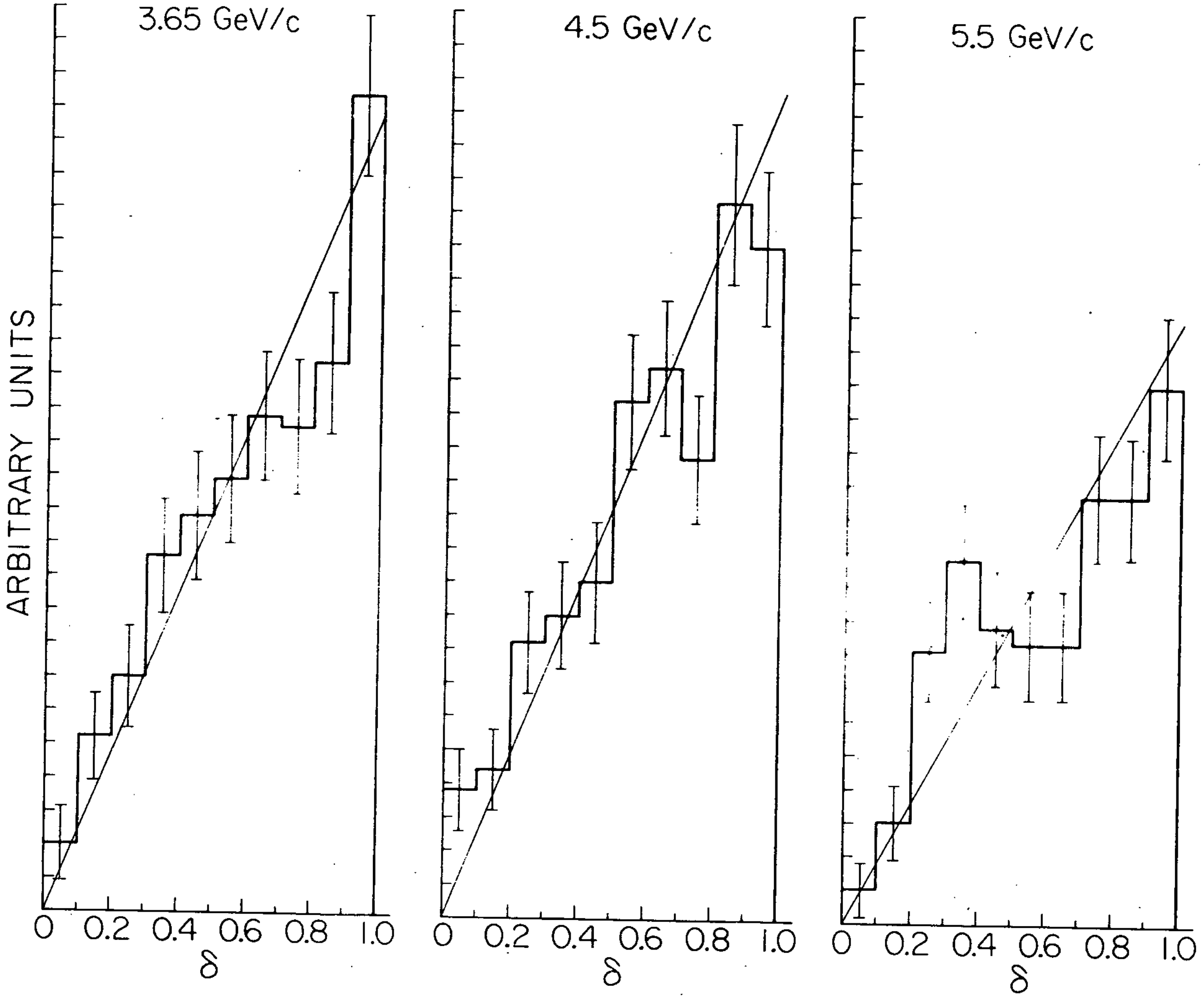

Figure IV.4. Vertex distributions along the beam for omega events.

VERTEX DISTRIBUTIONS ALONG BEAM
ω EVENTS (AFTER BACKGROUND SUBTRACTION)

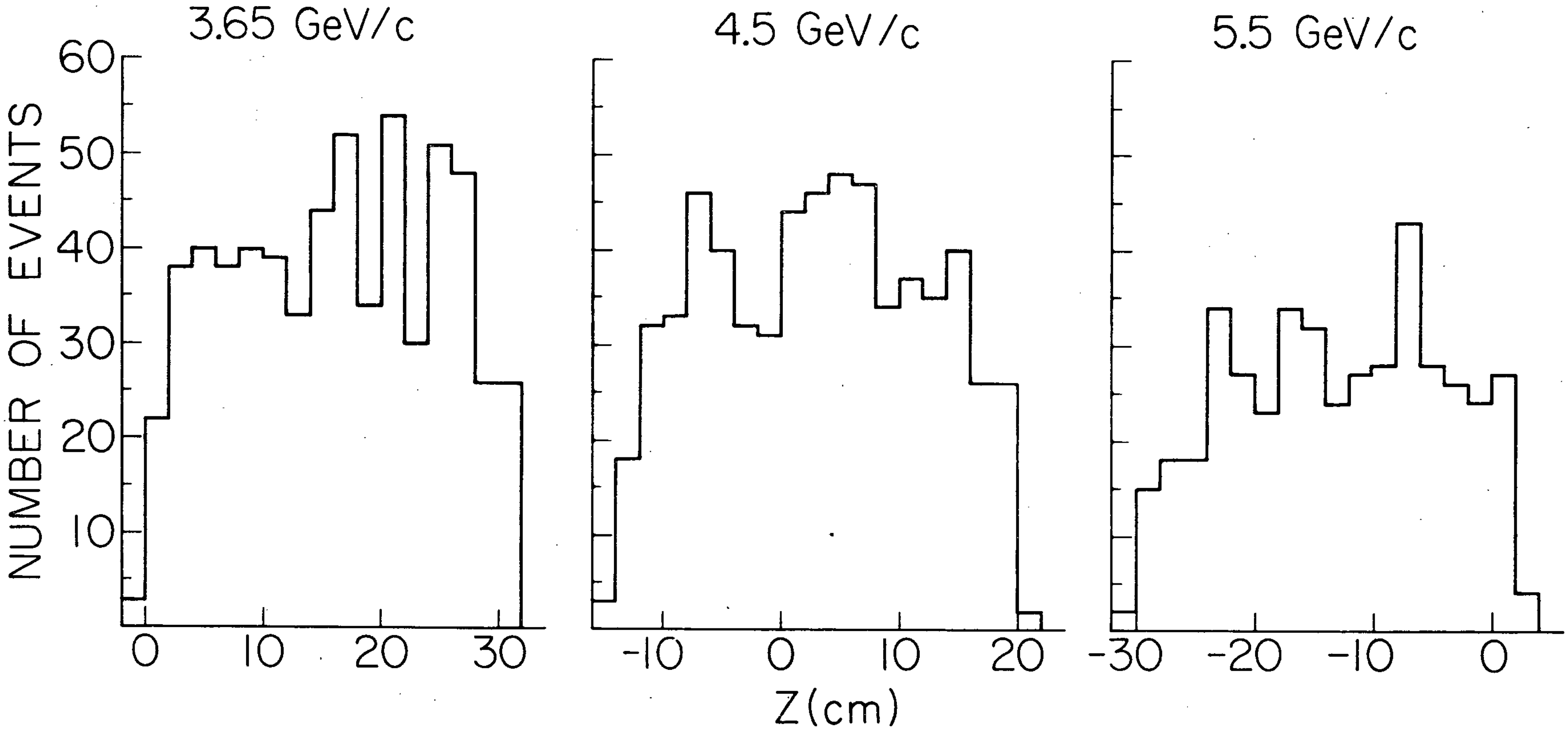

Figure IV.5. Vertex distributions along the beam for all reconstructed events.

VERTEX DISTRIBUTIONS ALONG BEAM
ALL FITTED EVENTS

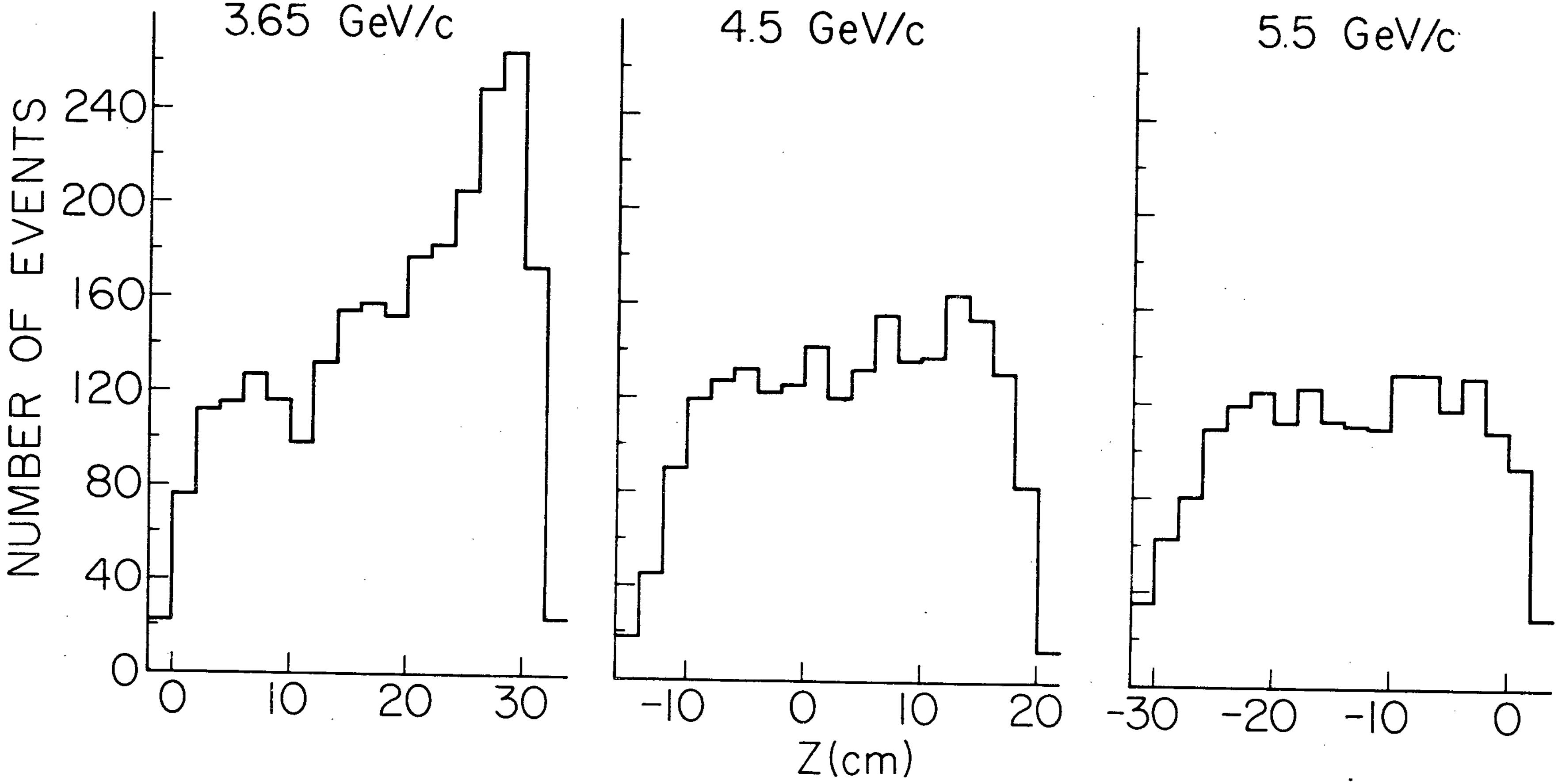

1. Biases dependent on the decay angles

A high statistics (30,000 events at each energy) Monte Carlo study assuming unpolarized omegas revealed the existance of an apparent polarization after processing the events through the standard energy and geometry cuts. This polarization exhibited a weak dependence on momentum transfer.

To correct for this bias, a weighting function of the form

$$W = \left[W_1 + \sum_{L=0}^{L_{max}} \sum_{M=-1}^{L} a_{LM} \, Y_{LM}(\theta,\phi) \right]^{-1} \qquad \text{(IV.5)}$$

(θ and ϕ are the decay angles in the Gottfried-Jackson frame) was constructed and used to assign an appropriate weight to each event. The term W_1 contains the momentum transfer dependence and is given by

$$W_1 = 1 + (0.020 + 0.070t - 0.006/t) \, Y_{20}(\theta,\phi) \qquad \text{(IV.6)}$$

at all three energies. The coefficients a_{LM} are independent of momentum transfer but change from energy to energy. It was found necessary to use terms through L=4 to remove the polarization. The $\cos\theta$ and ϕ distributions, weighted by (IV.5), for the Monte Carlo samples of unpolarized omegas are shown in Figure IV.6. They are consistent with the flat distributions expected.

An additional 30,000 Monte Carlo events were generated at each energy assuming a non-zero polarization. The specified values of the density matrix elements were $\rho_{00} = 0.3$, $\rho_{1-1} = 0.2$ and $\text{Re}(\rho_{10}) = 0.0$. These should be compared with the values obtained by processing these events through the analysis programs. These values are summarized in Table IV.1. We conclude that this procedure adequately compensates for the biases dependent on the decay angles.

Figure IV.6. Distributions in $\cos\theta$ and ϕ for the Monte Carlo samples of omega events generated assuming zero polarization. The events have been subjected to the standard geometry and energy cuts and weighted by (IV.5). The results are consistent with the expected flat distributions.

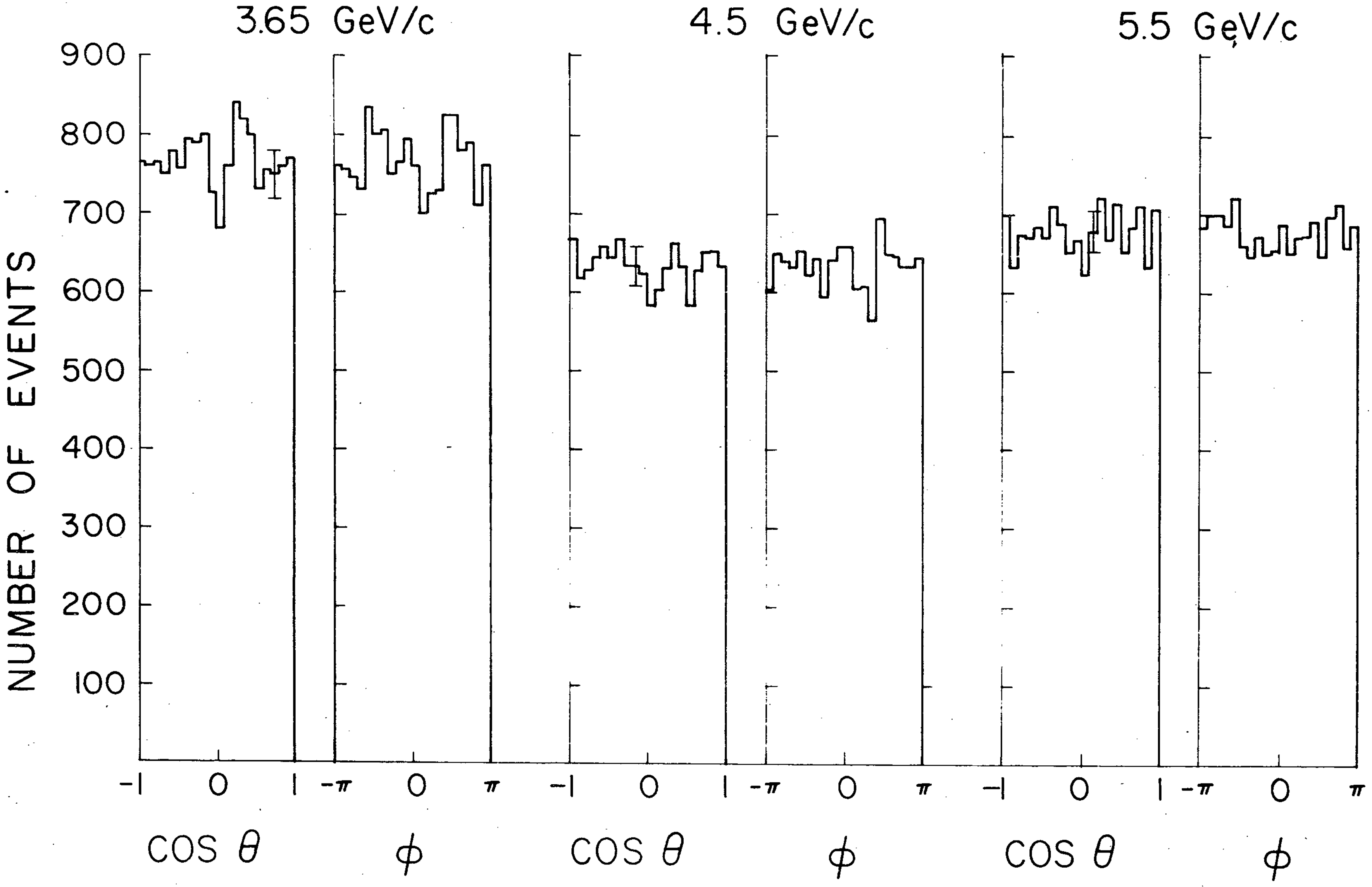
3.65 GeV/c
4.5 GeV/c
5.5 GeV/c
NUMBER OF EVENTS
900
800
700
600
500
400
300
200
100
-1
0
1
-π
0
π
-1
0
1
-π
0
π
-1
0
1
-π
0
π
COS θ
φ
COS θ
φ
COS θ
φ

Table IV.1

Results of analysis of Monte Carlo distributions. The omega was given a non-zero polarization. The input values of the density matrices were ρ_{00} = 0. 3, ρ_{1-1} = 0.2 and Re(ρ_{10}) = 0.0.

	3.65 GeV/c	4.5 GeV/c	5.5 GeV/c
ρ_{00}	0.302 ± 0.007	0.318 ± 0.007	0.335 ± 0.007
ρ_{1-1}	0.216 ± 0.006	0.210 ± 0.006	0.204 ± 0.005
Re(ρ_{10})	-0.004 ± 0.003	0.003 ± 0.003	0.003 ± 0.003

2. Biases dependent on momentum transfer

A Monte Carlo study, based on 5000 events at each energy was made to examine losses due to inefficiencies in the kinematic fitting program. The generated events were assigned errors corresponding to the known measurement errors and then processed by the fitting program. The fraction of events giving a successful kinematic fit varied smoothly with t (see Figure IV.7a) from ~ 0.80 at t= -0.05 $(GeV/c)^2$ to ~ 0.95 for t= -1.0 $(GeV/c)^2$.

The geometric acceptance of the meson arm of the experiment (the spark chambers and all counters except the neutron counter hodoscope) also showed a marked t-dependence. This acceptance varied smoothly from ~ 0.5 at small $|t|$ to ~ 0.65 at $|t|$ ~ 1. $(GeV/c)^2$ (Figure IV.7b).

In the neutron counter hodoscope the vertical banks of 4 counters were separated by 2 counter widths giving rise to an acceptance of ~ 1/3. A direct calculation of this effect, averaging over the target

Figure IV.7. (a) Fraction of modified Monte Carlo omega events which gave a satisfactory kinematic fit.

(b) Fraction of Monte Carlo omega events which appeared as two shower events in the meson arm.

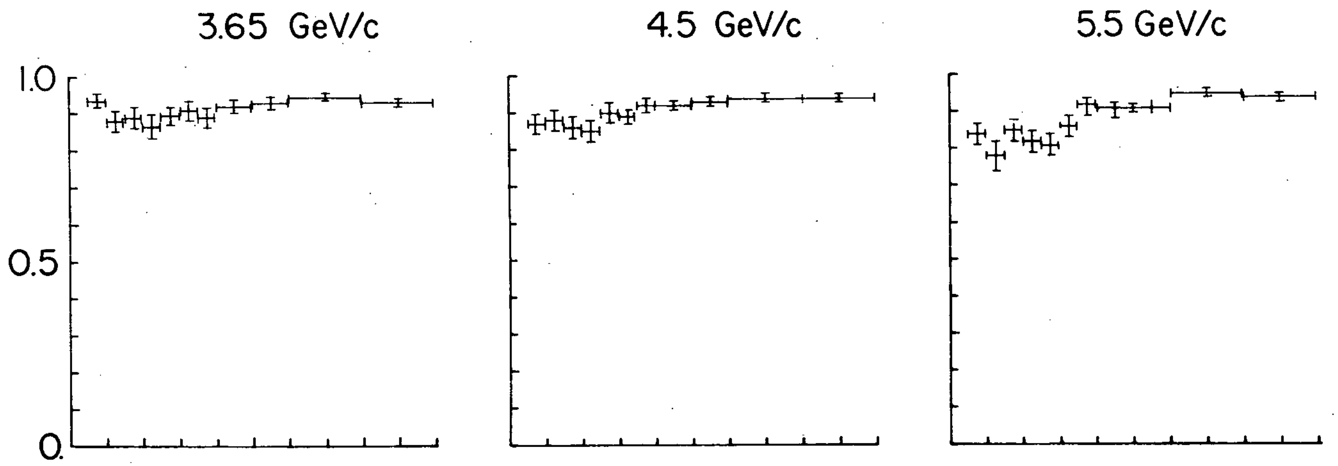

(a) EFFICIENCY OF KINEMATIC FITTING PROGRAM FOR TWO SHOWER EVENTS

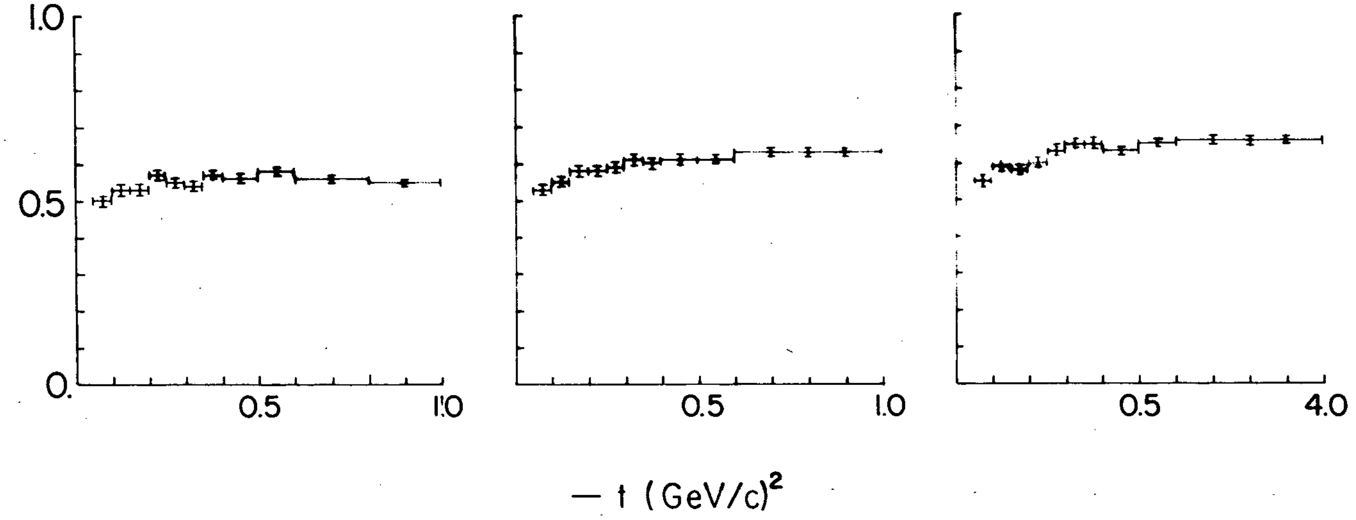

(b) GEOMETRIC EFFICIENCY FOR DETECTING 2 CHARGED πs & TWO GAMMAS length and the counter positions showed that this acceptance varied slightly with the neutron's laboratory angle, i.e., with t. The results of these calculations are summarized in Table IV.2.

Table IV.2

Neutron counter geometric acceptance averaged over target length and appropriate momentum transfer intervals.

-t	3.65 GeV/c	4.5 GeV/c	5.5 GeV/c
.05 - .1	0.288	0.297	0.293
.1 - 1.5	0.296	0.307	0.290
.15 - .2	0.304	0.292	0.296
.2 - .25	0.297	0.297	0.300
.25 - .3	0.284	0.297	0.295
.3 - .35	0.282	0.284	0.297
.35 - .4	0.280	0.289	0.286
.4 - .5	0.268	0.283	0.280
.5 - .6	0.298	0.289	0.292
.6 - .8	0.291	0.289	0.292
.8 - 1.0	0.286	0.294	0.299

E. Neutron Counter Efficiency

The detection of neutrons in scintillation counters depends on the occurance of nuclear interactions which produce charged secondaries or gammas which can produce an electron-positron pair. Consequently, the detection efficiency is expected to be energy dependent. A number of experimental studies[13-18] have shown that below a kinetic energy of 100 MeV the detection efficiency is strongly dependent on the kinetic energy and the energy threshhold. From 100 to several hundred MeV the detection efficiency is observed to be relatively constant at approximately 1% per cm of scintillator. This may be understood from two facts: essentially all n-p interactions and all inelastic n-C interactions in this energy range give light-producing secondaries; and the total cross sections are relatively constant. In this experiment the neutron kinetic energies range from 20 to 540 MeV.

A computer program has been developed by Kurz[19] to calculate the efficiency of plastic scintillators for detecting neutrons in the energy range 1 to 300 MeV. This program uses the available differential cross sections for n-p scattering and total cross sections for the various n-C channels. The response of plastic scintillator (specifically, NE102) as calculated and measured by Gooding and Pugh[20] is used in the calculation.

Kurz estimates an error of 10% on the calculated results and presents measured results for comparison. A number of other groups[13-18] have reported similar comparisons, and the agreement is generally adequate. The efficiency functions for our counters, calculated for thresholds of 4, 6, 8 and 10 MeV, are shown in Figure IV.8.

To support the use of the calculated neutron counter efficiencies in the analysis, a short experiment was performed to study the reaction

$$\pi^- p \rightarrow \pi^0 n \qquad \text{(IV.7)}$$

at 1.44 GeV/c. This energy was chosen to correspond to a recent measurement of the differential cross section for reaction (IV.7) and because the total cross section of 2.1 mb[21] would provide a reasonable data

Figure IV.8. Efficiencies calculated by Kurz's program for the counters used in this experiment. The results above 300 MeV are extrapolated from the results given by the program up to 300 MeV.

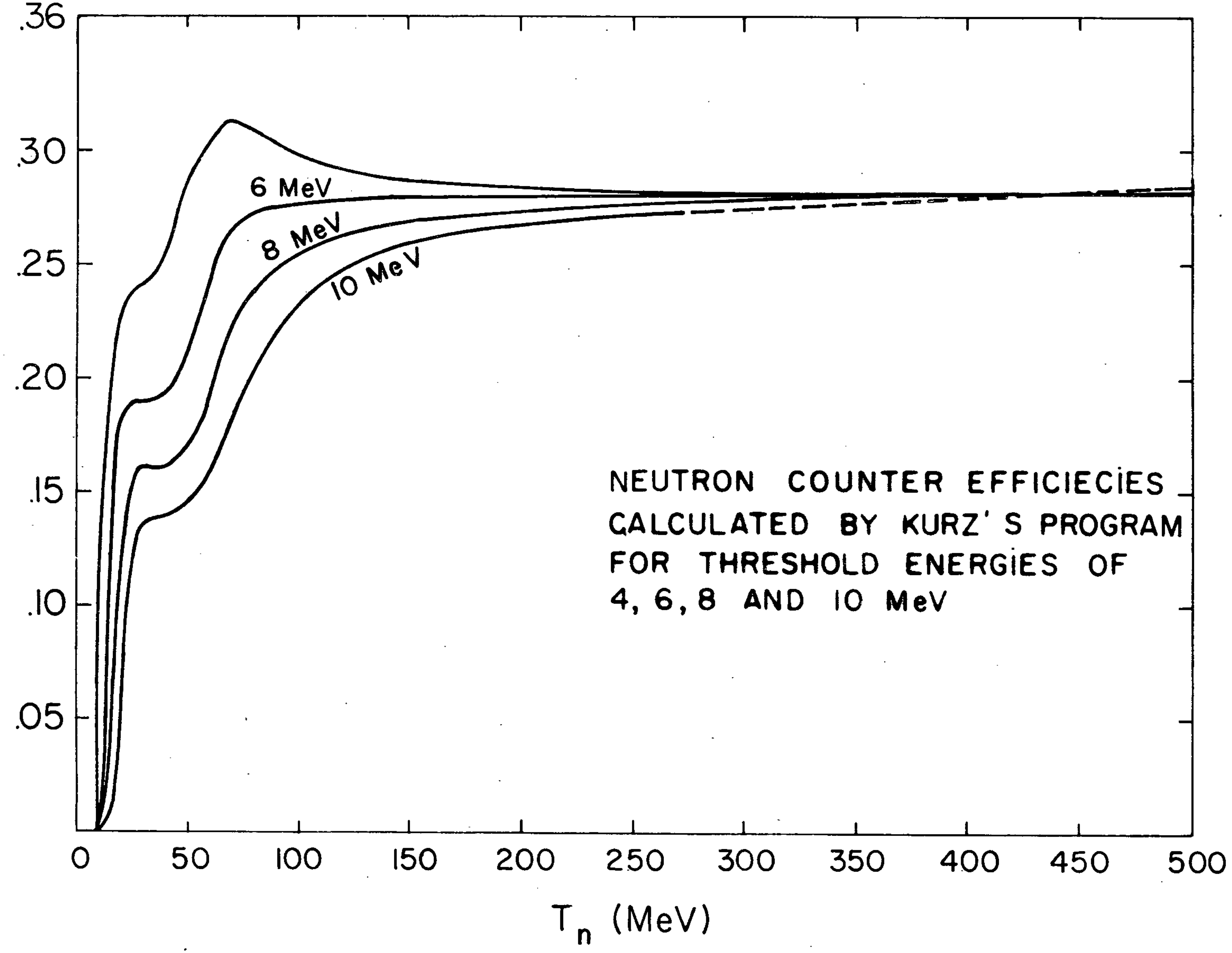

NEUTRON COUNTER EFFICIECIES
CALCULATED BY KURZ'S PROGRAM
FOR THRESHOLD ENERGIES OF
4, 6, 8 AND 10 MeV

rate. To further enhance the data rate, the neutron counters were placed approximately 5 m from the target. A minor change in the trigger logic used the π-hodoscope as an anti-counter and demanded an all-neutral final state.

In addition to reaction (IV.7), in four counters (θ's 10-13) the reaction

$$\pi^- p \rightarrow \eta^o n \qquad \text{(IV.8)}$$

was seen. Two typical time-of-flight spectra are shown in Figure IV.9, one, $\theta 9$, showing the prompt and π^o peaks, and the other, $\theta 11$, also showing the η^o peak.

The angular acceptance of the neutron counters corresponded to non-overlapping neutron kinetic energy intervals. The counter efficiencies were determined by calculating the expected counts in each counter and comparing with the number of events obtained from the time-of-flight spectra after a background subtraction. Internal consistency was provided by using a least-squares program to fit a polynomial to the background and Gaussians to the π^o and η^o peaks.

During this analysis, serious inconsistencies were found between the data of Chiu, et al.[21/] (including the data at 1.44 GeV/c) and the results of other experiments at similar energies. These problems are discussed in APPENDIX B.

The neutron counter thresholds were measured independently to be 6 MeV. In Figure IV.10 the calculated efficiency for a 6 MeV threshold is shown together with the measured efficiencies. The measured results are based on the data by Crouch, et al.[22/] The errors include

Figure IV.9. Typical time-of-flight spectra obtained on-line during the $\pi^- p$ charge-exchange run.

(a) The prompt peak and the peak due to $\pi^- p$ charge exchange scattering are visible.

(b) The peak due to η^o production is also visible.

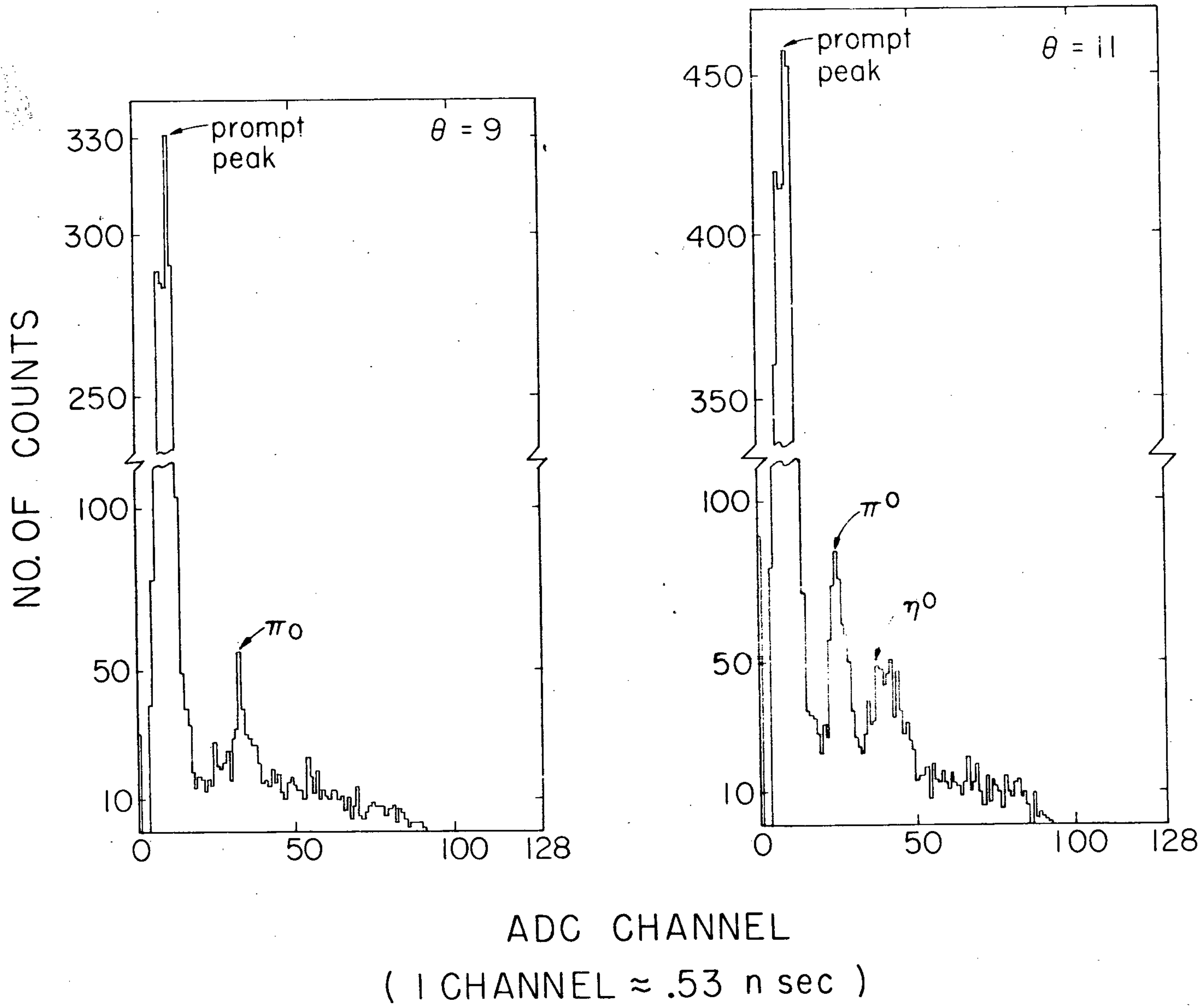
prompt peak
θ = 9
π0
330
300
250
100
50
10
0
50
100
128
NO. OF COUNTS
prompt peak
θ = 11
π0
η0
450
400
350
100
50
10
0
50
100
128
ADC CHANNEL
(1 CHANNEL ≈ .53 n sec)

Figure IV.10. Measured efficiencies based on charge-exchange data from Crouch, et al. The curve is calculated for a 6 MeV threshold.

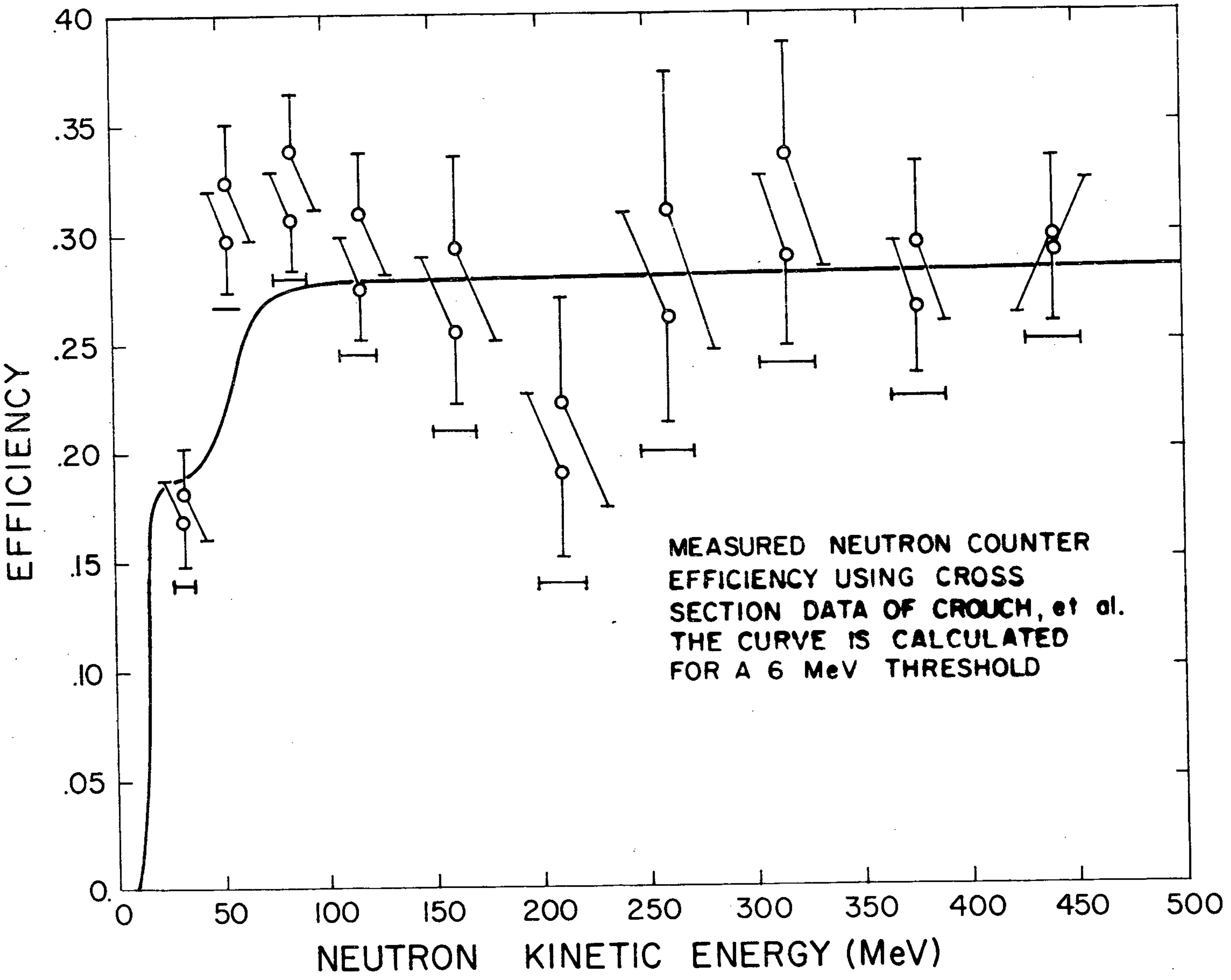

MEASURED NEUTRON COUNTER EFFICIENCY USING CROSS SECTION DATA OF CROUCH, et al. THE CURVE IS CALCULATED FOR A 6 MeV THRESHOLD both the statistical error and the published errors on the cross section data. One should also keep in mind the estimated 10% uncertainty in the calculated curve. We believe that the generally good agreement justifies the use of the calculated efficiency and all reported results use the result of the Kurz program.

V. RESULTS AND CONCLUSIONS

Momentum transfer distributions with each event weighted by

$$WT = 2\pi W/(\varepsilon_{NC}\Delta\phi) \tag{V.1}$$

were accumulated for both the ω mass region and adjacent control regions. The mass resolution of the experiment varied with t and the widths of the ω and control regions varied correspondingly. In (V.1), W is obtained from (IV.5), ε_{NC} is the calculated neutron counter efficiency shown in Figure IV.10 and $\Delta\phi/2\pi$ is the fraction of the azimuthal angle subtended by the neutron counters. The weighted distributions for the ω events were obtained by a simple straight-line background subtraction. All further discussion refers to the subtracted distributions.

The weighted distributions were used to obtain the total effective number, N_{eff}, of ω events produced in the target in each momentum transfer interval. Thus with Δn weighted events in the interval Δt,

$$\frac{N_{eff}}{\Delta t} = \frac{\Delta n}{\Delta t}\;\frac{1}{f_G f_K (f_{NC} f_{SC})}\;\frac{F}{f_E C_\gamma} \tag{V.2}$$

where f_G, f_K and f_{NC} are the meson arm geometric acceptance, the efficiency of the kinematic fitting program and the neutron counter geometric acceptance discussed in Section IV.D.2.

The recoil neutron passes through 2 cm LH_2, 1 cm scintillation plastic (CH), and 10 m air between the interaction vertex and the neutron counter. The factor f_{SC}, given in Table V.1, corrects for losses caused by scattering of the recoil neutron.

Table V.1

Correction factor for losses caused by scattering of recoil neutron.

$-t$	f_{SC}
.05 - .10	.85
.10 - .15	.91
.15 - .20	.94
.20 - 1.0	.96

Small losses caused by electronic inefficiencies are corrected for by f_E. These losses were measured to be 3% at all energies; $f_E = 0.97$.

The gammas from the π^o decay must pass through about 10 cm LH_2, 0.25 cm Al and 1 cm scintillation plastic up to and including the π-hodoscope. In passing through this material 12% of the photons will convert to an electron-positron pair and effectively veto the event by providing a third charged particle in the π- hodoscope. The factor C_γ corrects for this loss.

The missing mass spectrometer results were used to obtain a cross section normalization that is independent of scanning and measuring biases. The number of ω events detected in the spectrometer, N_{spec}, was determined by fitting a straight line to the background and a Gaussian to the ω peak. The width of the Gaussian was constrained to the known spectrometer mass resolution. To avoid problems with the neutron counter efficiency at low t and the poor signal-to-noise ratio at high t, only the interval $0.15\ (\mathrm{GeV}/c)^2 \leq |t| \leq 0.60\ (\mathrm{GeV}/c)^2$ was used. Using the number of events in this t interval which survived fitting and selection, N_{fit}, we obtain

$$F = \frac{N_{spec} \left\langle f_{2\gamma} \right\rangle \left\langle f_K \right\rangle}{N_{fit}} \tag{V.3}$$

Here, $\left\langle f_{2\gamma} \right\rangle$ is the probability of both gammas from an ω decay hitting in the fiducial volume ($f_{2\gamma} \sim 70\%$) and $\left\langle f_K \right\rangle$ is the efficiency of the fitting programs, both averaged over the momentum transfer interval.

The cross sections calculated from our data are corrected for the fact that $\omega \rightarrow \pi^+\pi^-\pi^o$ only (89.8 ± 4.0)% of the time. In addition, to facilitate comparison with existing data, we assume that the contribution from the interval $|t| \leq 0.05$ $(\text{GeV/c})^2$ is 90% of that from the interval 0.05 $(\text{GeV/c})^2 \leq |t| \leq 0.10$ $(\text{GeV/c})^2$. The total cross sections are (0.29 ± .02), (0.19 ± .01) and (0.12 ± 0.01 mb at 3.65, 4.5 and 5.5 GeV/c respectively. The errors include only the statistical uncertainty. They do not include the overall normalization uncertainty. In Figure V.1 we have plotted the available total cross sections for ω production at p_{lab} = 1.7,[23] 2.7,[24] 4.1,[25] 5.1,[26] 5.4[27] and 6.95[28] GeV/c. The straight line through these data points is a free-hand estimate. It is clear that our results are inconsistent with the other data.

We can conjecture two possible mechanisms to account for this apparent loss of events. In the liquid hydrogen target, the incident π^- beam particles and the charged π's from the ω decay will produce δ-rays having energy greater than E at a rate 0.01/E per cm path length.[29] To estimate the magnitude of this effect we use the minimum dE/dx for electrons in liquid hydrogen, ~ 0.29 MeV/cm, and assume that a minimum

Figure V.1. Total cross sections for $\pi^- p \rightarrow \omega n$ from 1.7 to 6.95 GeV/c. References are given in the text. The errors shown for the points from this experiment do not include the estimated 20% normalization uncertainty.

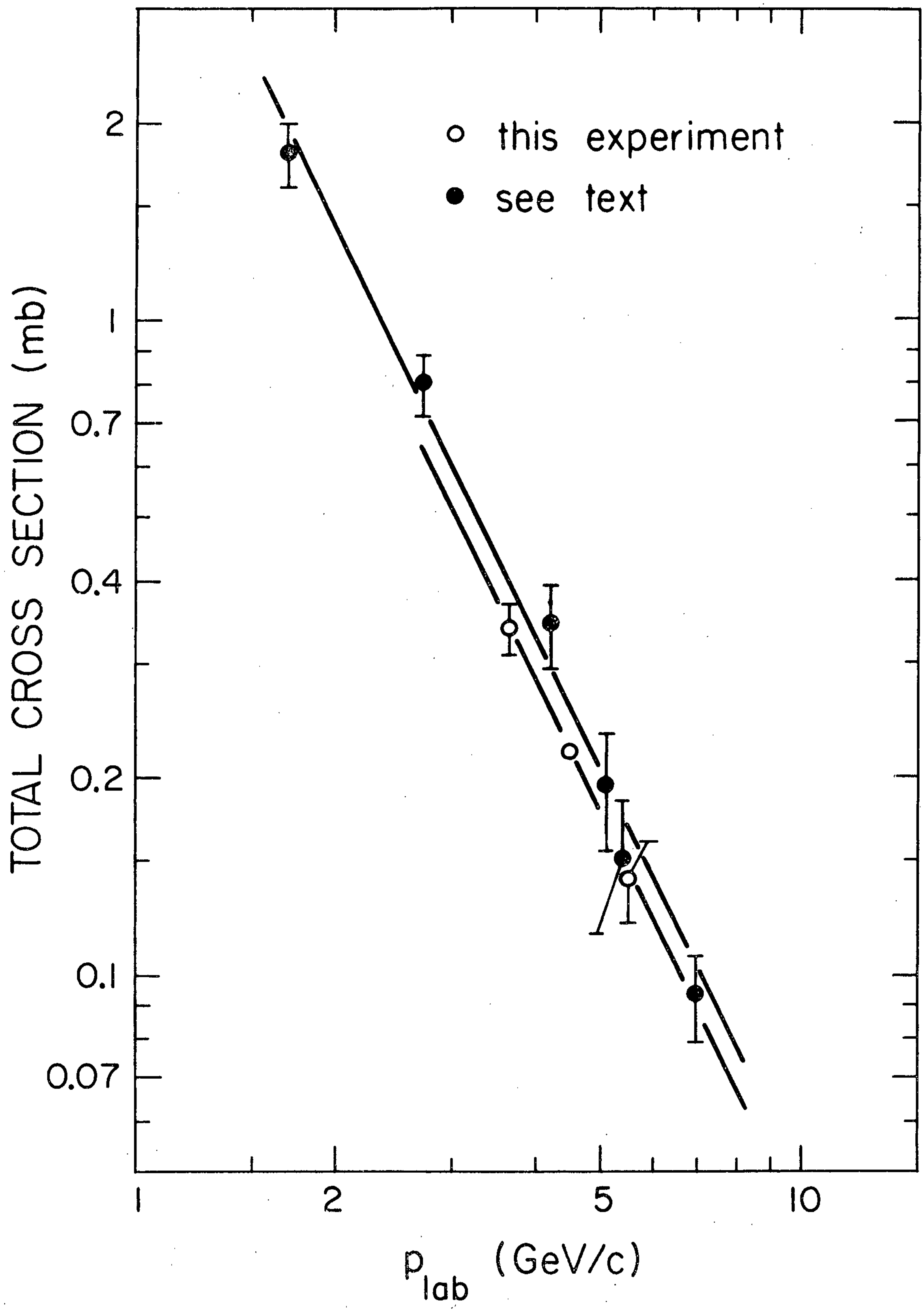
TOTAL CROSS SECTION (mb)
2
1
0.7
0.4
0.2
0.1
0.07
1
2
5
10
p_{lab} (GeV/c)
○ this experiment
● see text

electron energy of 0.5 MeV is required to trigger the π-counters. The minimum required energy is then

$$E = 0.5 + 0.29\ (30 - x) \tag{V.4}$$

for a δ-ray passing through x cm of liquid hydrogen. The average number of δ-rays capable of triggering a π counter produced by a π passing through the target (30 cm hydrogen) is

$$\langle n \rangle = \int_0^{30} dx\, \frac{0.01}{0.5 + 0.29\ (30 - x)} = 0.1\ . \tag{V.5}$$

Taking an average charged π path length of 45 cm, we have 0.15 δ-rays per event capable of triggering the π-hodoscope and violating the 2π requirement. For charged π's emerging from the interaction away from the forward direction, the fact that they must now pass through the aluminum can surrounding the target (see Figure III.2) compensates for the reduced path length in the hydrogen. We estimate the uncertainty in this calculation to be ± 0.1. The cross section data shown in Figure V.1 - V.4 include the correction for this 15% loss. The resulting total cross sections are (0.34 ± 0.03), (0.22 ± 0.02) and (0.14 ± 0.02) mb at 3.65, 4.5 and 5.5 GeV/c. The quoted errors include only the relative (statistical) uncertainty. We estimate there is an additional 20% normalization uncertainty.

The charged π's and γ's from ω events can interact in the shower chambers. Such interactions will sometimes produce backward-going charged secondaries which reach either the π-hodoscope (violating the 2π requirement) or an anti counter. In either case, the event is lost. We are unable to make a reliable estimate of the magnitude of this effect but 5% to 10% would not be unreasonable.

Figure V.2. dσ/dt at 3.65 GeV/c. The errors shown include only the relative error. There is an additional 20% normalization uncertainty.

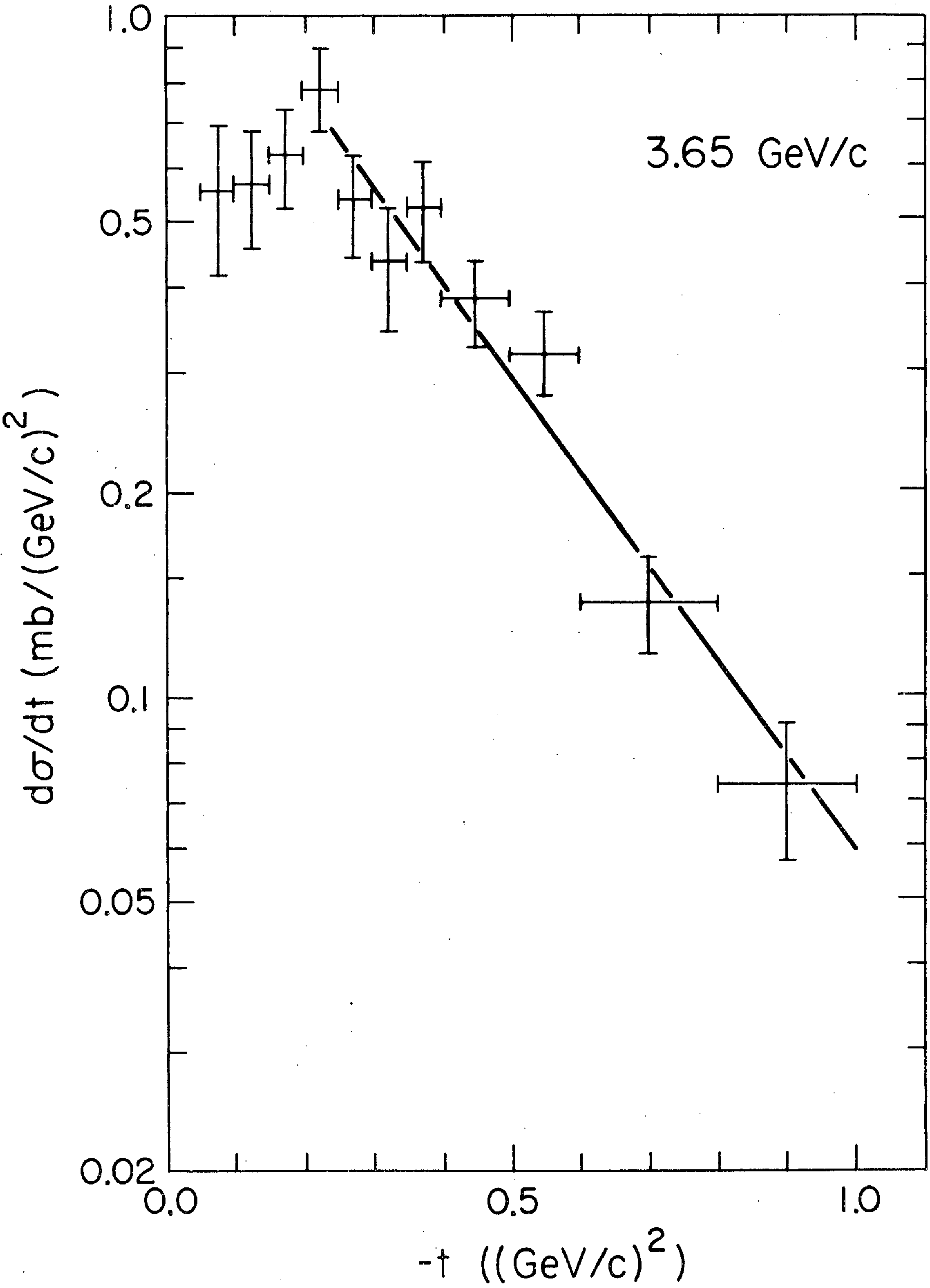

1.0
0.5
0.2
0.1
0.05
0.02
0.0
0.5
1.0
3.65 GeV/c
dσ/dt (mb/(GeV/c)^2)
-t ((GeV/c)^2)

Figure V.3. $d\sigma/dt$ at 4.5 GeV/c. The errors shown include only the relative error. There is an additional 20% normalization uncertainty.

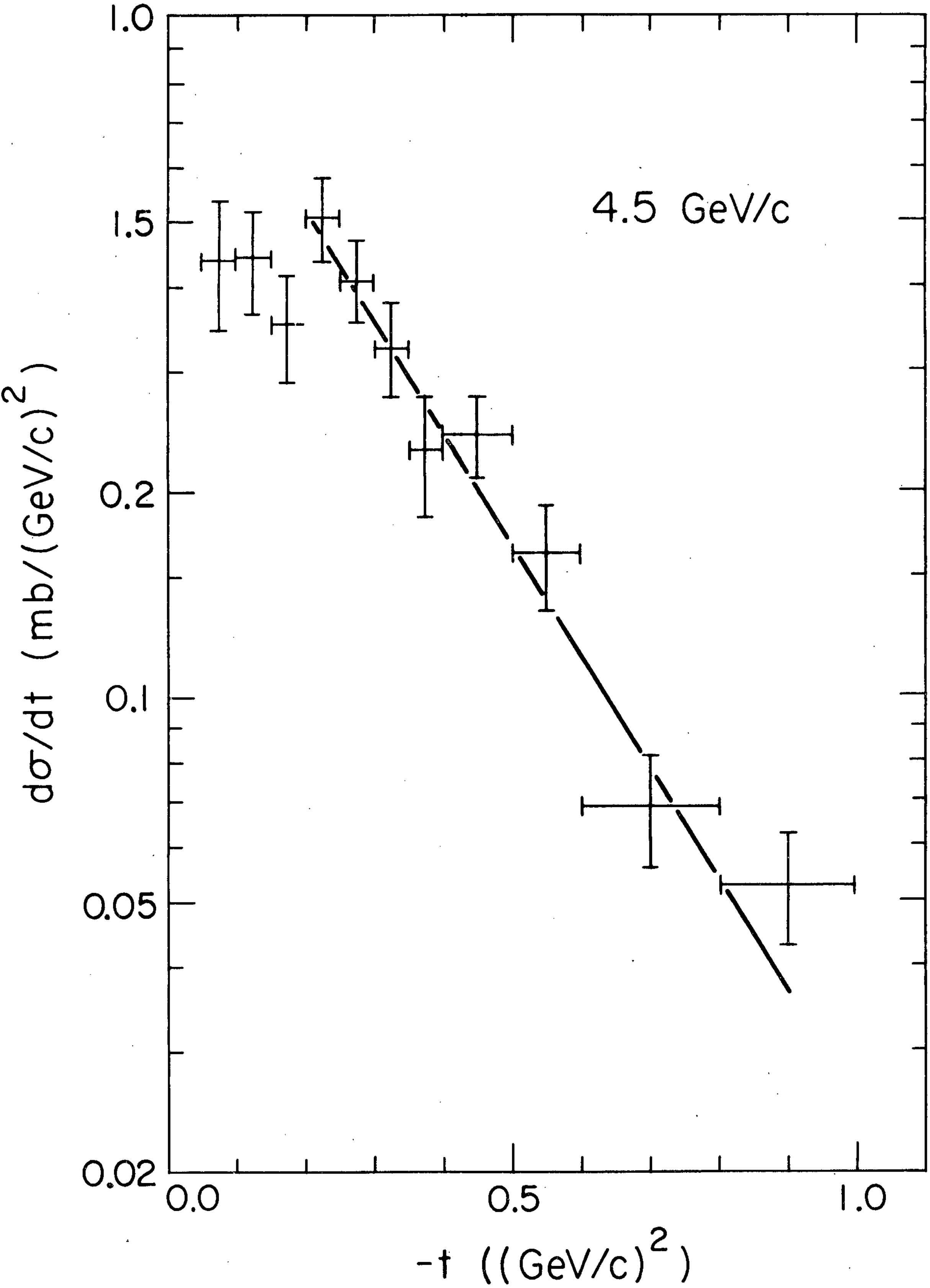
4.5 GeV/c
$d\sigma/dt$ (mb/(GeV/c)^2)
1.0
1.5
0.2
0.1
0.05
0.02
0.0
0.5
1.0
$-t$ ((GeV/c)^2)

Figure V.4. dσ/dt at 5.5 GeV/c. The errors shown include only the relative error. There is an additional 20% normalization uncertainty.

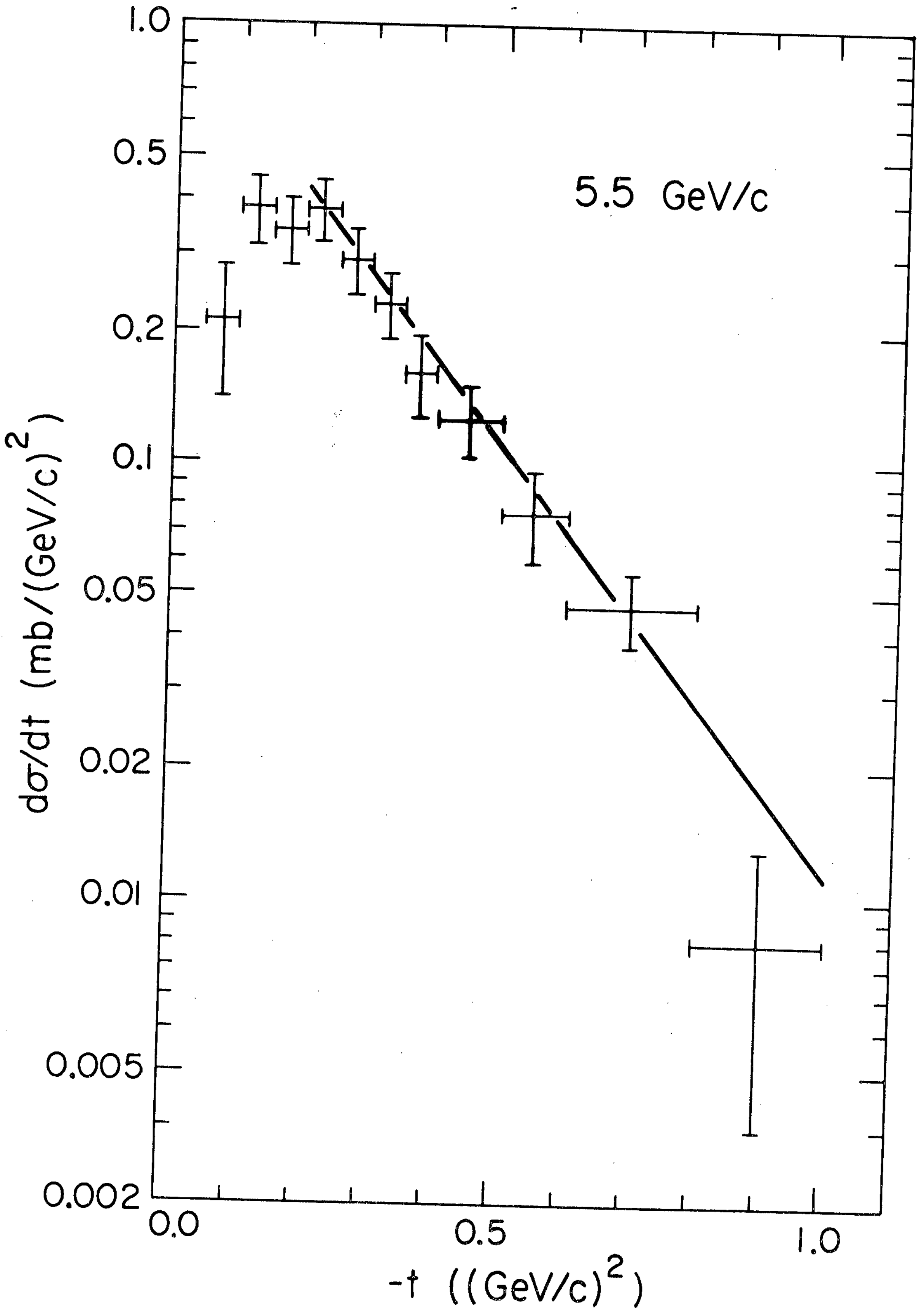
5.5 GeV/c
dσ/dt (mb/(GeV/c)^2)
-t ((GeV/c)^2)
1.0
0.5
0.2
0.1
0.05
0.02
0.01
0.005
0.002
0.0
0.5
1.0

At the energies used in this experiment these effects are expected to be energy independent and so would not affect the observed energy dependence of the total cross sections. The energy dependence of our data, shown in Figure V.1, is in excellent agreement with that of the other data.

The differential cross sections are shown in Figures V.2 - V.4 and summarized in Table V.2. The general features are in agreement with the previously reported data. There is a dip, becoming more pronounced with increasing energy, in the forward direction. For $t \leq -0.25$ $(\text{GeV}/c)^2$ the cross section falls smoothly. The slope increases with energy. A fit of $d\sigma/dt$ to the form Ae^{Bt} in the momentum transfer interval -1.0 $(\text{GeV}/c)^2 \leq t \leq -0.25$ $(\text{GeV}/c)^2$ gives $B = 3.2 \pm 0.3$, 3.6 ± 0.3, and 4.9 ± 0.5 $(\text{GeV}/c)^{-2}$ at 3.65, 4.5 and 5.5 GeV/c respectively. There is no evidence for a dip in $d\sigma/dt$ at $t \sim -0.6$ $(\text{GeV}/c)^2$.

The calculation of the ω spin density matrix elements has been discussed in detail elsewhere.[12/] The results are presented in Figure V.5 - V.8 and Table V.3 for completeness. We note two important features of those data. The large values of ρ_{00} and $\rho_{11} - \rho_{1-1}$ require a strong unnatural parity contribution to the production amplitudes. The lack of any indication of a dip in $\rho_{11} + \rho_{1-1}$ at $t \sim -0.6$ $(\text{GeV}/c)^2$ implies that either the ρ-trajectory is not the sole natural parity contribution to the process or there is no wrong signature nonsense zero in the ρ-trajectory contribution to the scattering amplitude.

The energy dependences of the natural and unnatural parity parts of the total cross section are shown in Figure V.9. These results agree

Table V.2

Differential cross section in mb/(GeV/c)^2. Errors do not include the estimated 20% normalization uncertainty.

$-t(\mathrm{GeV}/c)^2$	3.65 GeV/c	4.5 GeV/c	5.5 GeV/c
0.05 - 0.10	0.55 ± 0.14	0.44 ± 0.09	0.21 ± 0.07
0.10 - 0.15	0.57 ± 0.11	0.44 ± 0.07	0.38 ± 0.07
0.15 - 0.20	0.62 ± 0.10	0.35 ± 0.06	0.34 ± 0.06
0.20 - 0.25	0.78 ± 0.11	0.51 ± 0.07	0.38 ± 0.06
0.25 - 0.30	0.53 ± 0.09	0.41 ± 0.06	0.29 ± 0.05
0.30 - 0.35	0.43 ± 0.09	0.32 ± 0.05	0.23 ± 0.04
0.35 - 0.40	0.52 ± 0.09	0.23 ± 0.05	0.16 ± 0.03
0.40 - 0.50	0.38 ± 0.06	0.24 ± 0.03	0.13 ± 0.02
0.50 - 0.60	0.32 ± 0.04	0.16 ± 0.03	0.077 ± 0.018
0.60 - 0.80	0.14 ± 0.02	0.069 ± 0.013	0.047 ± 0.009
0.80 - 1.00	0.074 ± 0.017	0.053 ± 0.010	0.008 ± 0.005

Table V.3

Spin density matrix elements of the ω

Density Matrix Elements	-t	3.56 GeV/c	4.5 GeV/c	5.5 GeV/c	3.56 GeV/c	4.5 GeV/c	5.5 GeV/c
		Gottfried-Jackson Frame			Helicity Frame		
ρ_{00}	0.05 - 0.15	0.51 ± 0.11	0.28 ± 0.09	0.33 ± 0.11	0.29 ± 0.10	0.29 ± 0.10	0.35 ± 0.12
	0.15 - 0.25	0.27 ± 0.07	0.33 ± 0.07	0.29 ± 0.08	0.17 ± 0.07	0.28 ± 0.08	0.22 ± 0.07
	0.25 - 0.35	0.20 ± 0.10	0.22 ± 0.07	0.06 ± 0.08	0.42 ± 0.10	0.25 ± 0.07	0.29 ± 0.09
	0.35 - 0.50	0.25 ± 0.08	0.23 ± 0.07	0.11 ± 0.09	0.32 ± 0.08	0.28 ± 0.08	0.19 ± 0.09
	0.50 - 0.70	0.38 ± 0.09	0.28 ± 0.09	0.36 ± 0.13	0.22 ± 0.08	0.24 ± 0.09	0.12 ± 0.12
	0.70 - 1.00	0.48 ± 0.13	0.40 ± 0.13	0.67 ± 0.23	0.25 ± 0.11	0.17 ± 0.13	0.20 ± 0.18
ρ_{1-1}	0.05 - 0.15	0.26 ± 0.10	0.20 ± 0.08	0.16 ± 0.10	0.15 ± 0.10	0.20 ± 0.08	0.17 ± 0.11
	0.15 - 0.25	0.17 ± 0.07	0.19 ± 0.07	0.24 ± 0.07	0.12 ± 0.07	0.17 ± 0.07	0.20 ± 0.07
	0.25 - 0.35	0.05 ± 0.09	0.14 ± 0.07	0.21 ± 0.08	0.16 ± 0.09	0.15 ± 0.07	0.32 ± 0.08
	0.35 - 0.50	0.10 ± 0.07	0.11 ± 0.07	0.27 ± 0.09	0.13 ± 0.07	0.14 ± 0.07	0.31 ± 0.09
	0.50 - 0.70	0.07 ± 0.08	0.10 ± 0.09	0.19 ± 0.12	-0.01 ± 0.09	0.08 ± 0.09	0.07 ± 0.12
	0.70 - 1.00	-0.10 ± 0.09	0.01 ± 0.12	-0.01 ± 0.16	-0.22 ± 0.11	-0.11 ± 0.12	-0.24 ± 0.20
$\mathrm{Re}(\rho_{10})$	0.05 - 0.15	-0.04 ± 0.06	-0.04 ± 0.05	-0.06 ± 0.07	0.18 ± 0.06	0.03 ± 0.05	0.03 ± 0.06
	0.15 - 0.25	0.02 ± 0.04	-0.07 ± 0.04	-0.06 ± 0.04	0.00 ± 0.04	0.08 ± 0.04	0.08 ± 0.04
	0.25 - 0.35	-0.13 ± 0.05	-0.00 ± 0.04	-0.07 ± 0.05	0.09 ± 0.05	-0.01 ± 0.04	0.01 ± 0.05
	0.35 - 0.50	-0.14 ± 0.04	0.00 ± 0.04	-0.02 ± 0.05	0.13 ± 0.04	-0.02 ± 0.04	0.02 ± 0.05
	0.50 - 0.70	-0.12 ± 0.05	-0.11 ± 0.06	-0.10 ± 0.07	0.10 ± 0.05	0.09 ± 0.05	0.08 ± 0.07
	0.70 - 1.00	-0.20 ± 0.07	-0.21 ± 0.08	-0.09 ± 0.12	0.16 ± 0.07	0.17 ± 0.08	0.03 ± 0.13
		$\rho_{11} - \rho_{1-1}$ (Gottfried-Jackson Frame)			$\rho_{11} + \rho_{1-1}$ (both frames)		
	0.05 - 0.15	-0.01 ± 0.10	0.17 ± 0.08	0.18 ± 0.10	0.51 ± 0.12	0.57 ± 0.10	0.49 ± 0.13
	0.15 - 0.25	0.19 ± 0.07	0.15 ± 0.07	0.12 ± 0.06	0.54 ± 0.08	0.53 ± 0.09	0.60 ± 0.09
	0.25 - 0.35	0.35 ± 0.09	0.25 ± 0.07	0.26 ± 0.08	0.45 ± 0.11	0.53 ± 0.08	0.68 ± 0.10
	0.35 - 0.50	0.28 ± 0.08	0.27 ± 0.07	0.18 ± 0.09	0.47 ± 0.08	0.50 ± 0.08	0.72 ± 0.11
	0.50 - 0.70	0.24 ± 0.09	0.25 ± 0.09	0.12 ± 0.13	0.38 ± 0.10	0.46 ± 0.11	0.51 ± 0.14
	0.70 - 1.00	0.36 ± 0.11	0.29 ± 0.13	0.17 ± 0.18	0.16 ± 0.12	0.31 ± 0.14	0.16 ± 0.22

Figure V.5 Density matrix element ρ_{00}.

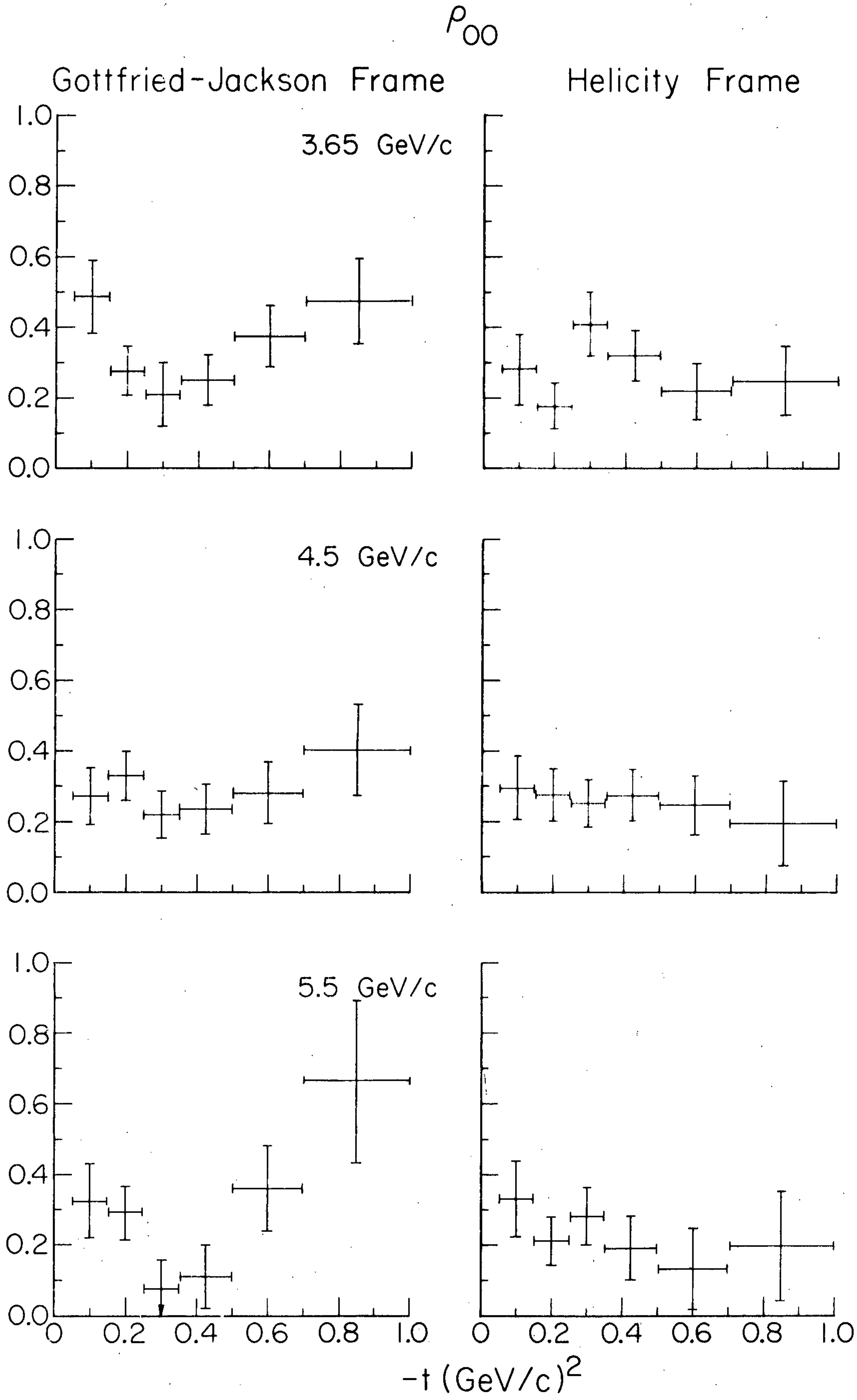
ρ_{00}
Gottfried-Jackson Frame
Helicity Frame
3.65 GeV/c
4.5 GeV/c
5.5 GeV/c
0.0
0.2
0.4
0.6
0.8
1.0
0
0.2
0.4
0.6
0.8
1.0
−t (GeV/c)^2

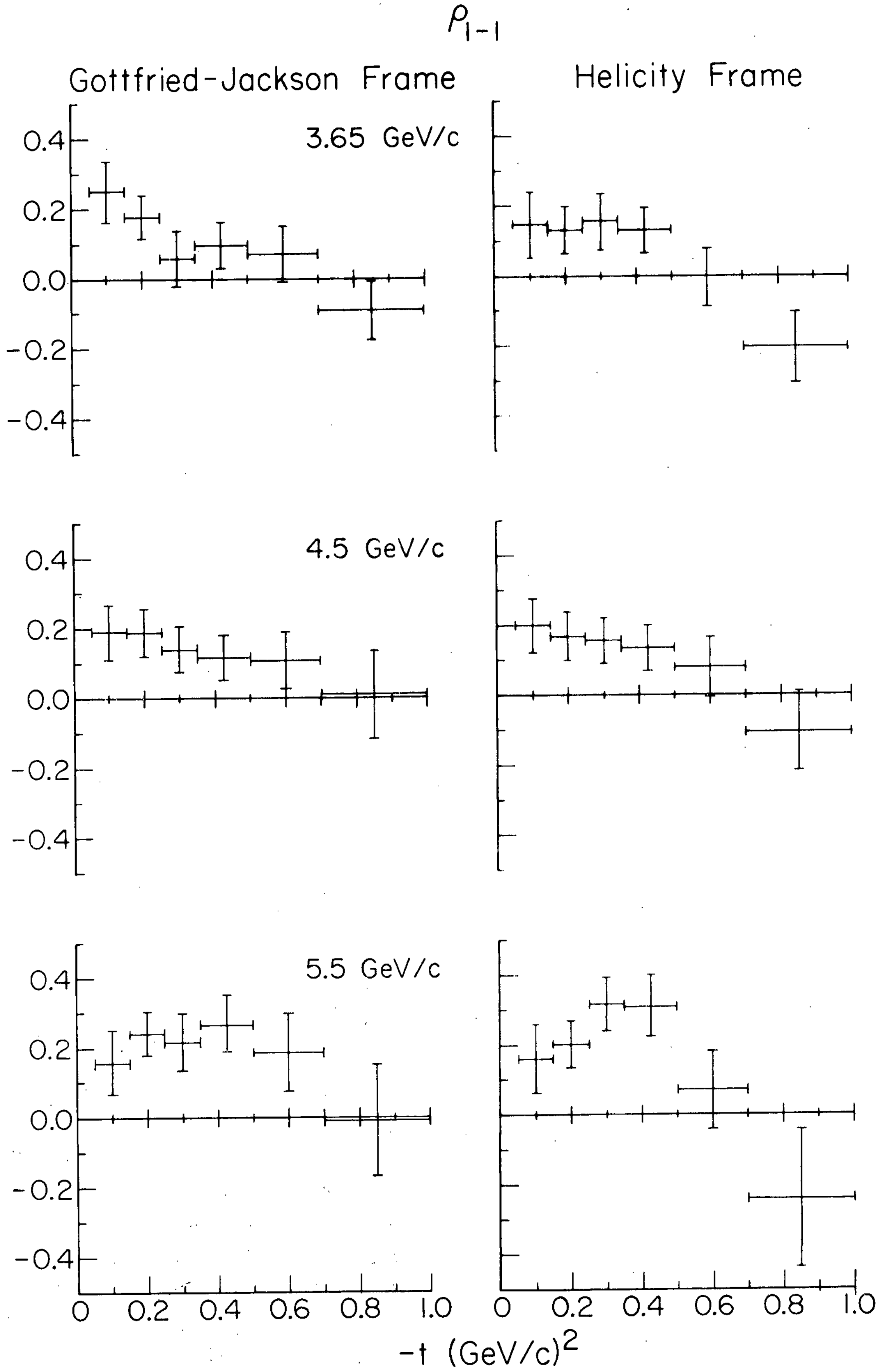
ρ_{1-1}
Gottfried-Jackson Frame
Helicity Frame
3.65 GeV/c
4.5 GeV/c
5.5 GeV/c
0.4
0.2
0.0
-0.2
-0.4
0
0.2
0.4
0.6
0.8
1.0
$-t\ (\mathrm{GeV}/c)^2$

Figure V.7. Density matrix element Re ρ_{10}. The limits obtained from the relation $2(\mathrm{Re}\ \rho_{10})^2 \leq \rho_{00}(\rho_{11}-\rho_{1-1})$ are indicated.

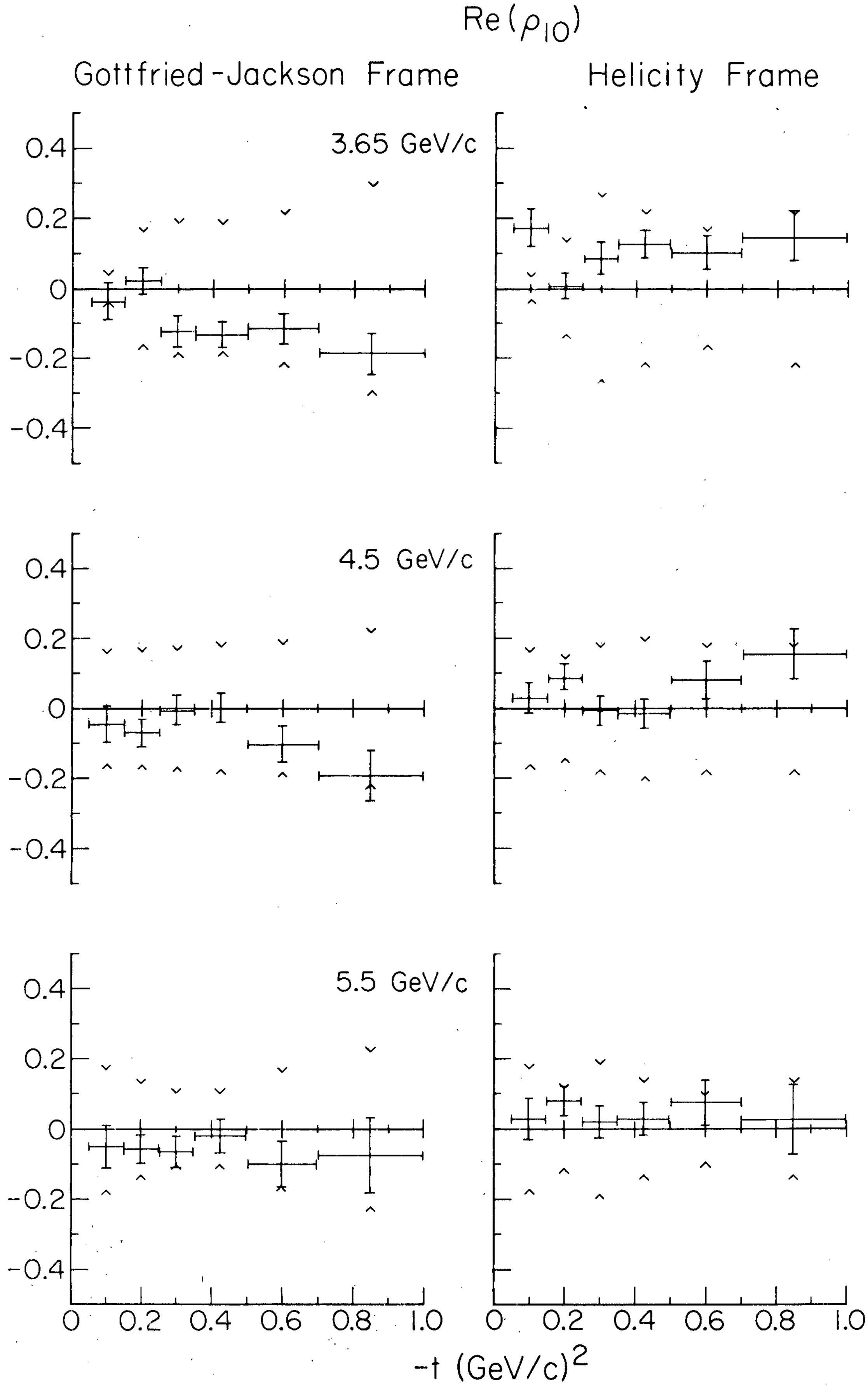
Re(ρ_{10})
Gottfried-Jackson Frame
Helicity Frame
3.65 GeV/c
4.5 GeV/c
5.5 GeV/c
0.4
0.2
0
-0.2
-0.4
0
0.2
0.4
0.6
0.8
1.0
-t (GeV/c)^2

Figure V.8. Density matrix elements $\rho_{11} \pm \rho_{1-1}$.

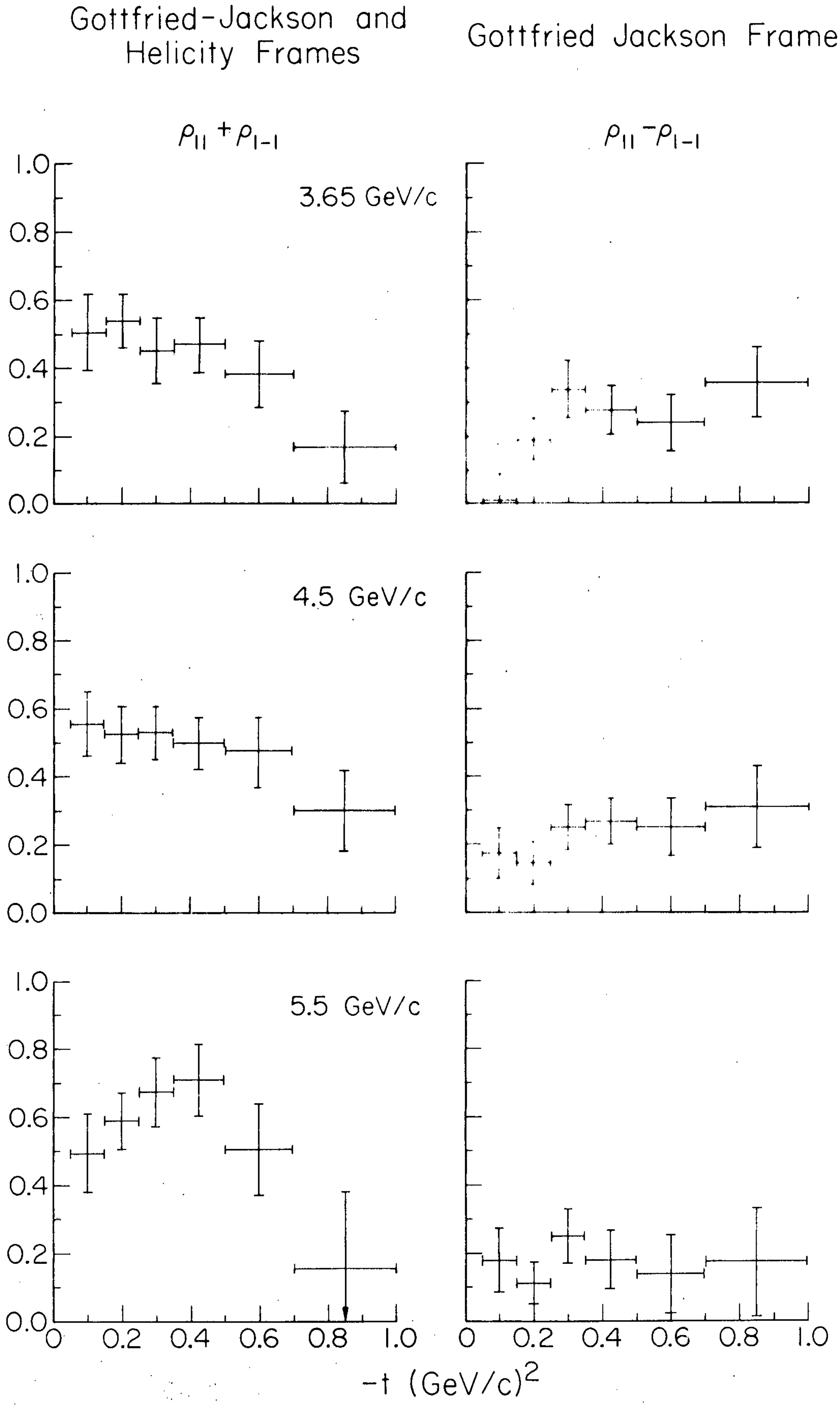
Gottfried-Jackson and Helicity Frames
Gottfried Jackson Frame
$\rho_{11}+\rho_{1-1}$
$\rho_{11}-\rho_{1-1}$
3.65 GeV/c
4.5 GeV/c
5.5 GeV/c
1.0
0.8
0.6
0.4
0.2
0.0
0
0.2
0.4
0.6
0.8
1.0
$-t\ (\mathrm{GeV}/c)^2$

Figure V.9. Energy dependence of natural and unnatural parity contributions to the total cross section.

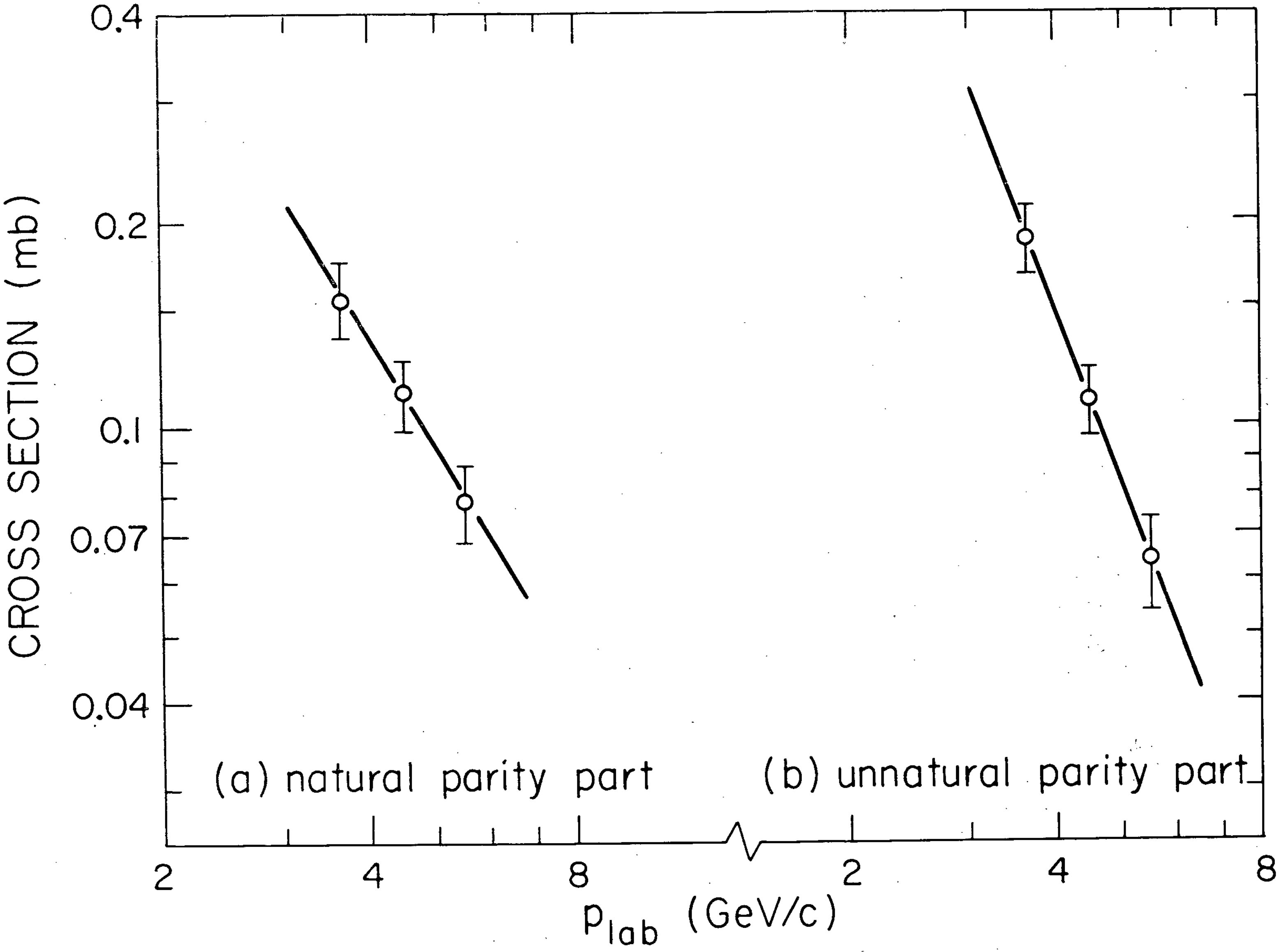

0.4
0.2
0.1
0.07
0.04
CROSS SECTION (mb)
(a) natural parity part
(b) unnatural parity part
2
4
8
2
4
8
p_{lab} (GeV/c)

with the qualitative features discussed in Chapter II. Using equation (II.8) we find that t=0 intercepts to be $\alpha_n(0) = 0.3 + 0.3$ and $\alpha_u(0) = -0.3 \pm 0.4$ for the natural and unnatural parity cases respectively. The commonly accepted value of the intercept of the ρ-trajectory is $\alpha_\rho(0) \sim 0.5$; of the B-trajectory, $\alpha_B(0) \sim -0.3$.

We conclude that the energy dependence of the data is consistent with that expected from simple Regge models. However, the other features of the data disagree strongly with the predictions of the simple Regge models discussed in Chapter II.

APPENDIX A

SUMMARY OF SCANNING AND MEASURING RESULTS

A total of 134,800, 142,700 and 148,100 events were recorded at 3.65, 4.5 and 5.5 GeV/c. After the prescan and scan cuts, 15,763, 11,711 and 11,184 events remained as 2γ ω candidates. The classification of events by the scanners, based on all events with a corrected spectrometer mass between 0.55 and 1.01 GeV, is summarized in Table A.1. This mass cut includes 54%, 41% and 35% of the events at the three energies. It is slightly stronger than the prescan cuts described in Section IV.A. The important observation is that the results in Table A.1 are consistent from energy to energy.

Table A.1

Classification of events by scanners

Class	3.65 GeV/c	4.5 GeV/c	5.5 GeV/c
0γ	49%	51%	56%
1γ	23%	20%	18%
2γ	19%	17%	16%
$\geq 3\gamma$	6%	9%	7%
breakdown	2%	2%	3%

During measuring and fitting, 35%, 30% and 36% of the events selected as 2γ ω candidates were rejected. These losses are summarized in Table A.2. The class "program rejects" contains events which the fitting program found to be internally inconsistent. The class "illegal events" contains events which were properly classified as to number of showers but where, for example, the interaction vertex is clearly downstream of the foil chambers.

Table A.2

Classification of measuring and fitting losses.

	3.65 GeV/c	4.5 GeV/c	5.5 GeV/c
Program rejects	18%	18%	20%
Scanner error	58%	56%	48%
Unmeasurable	15%	16%	22%
Illegal events	8%	10%	10%

An additional 20% of the events selected by the scanners failed to satisfy the χ^2, energy and geometry cuts after being processed by the fitting programs.

To estimate the efficiency of a single scan for selecting 2γ events, a portion of the film was scanned twice and the conflicts resolved. We find a single scan efficiency of 70% to 75% with a statistical uncertainty of 10%. Inherent in this analysis are the assumptions that there are no qualitative differences between the events found by a scanner and those missed and that the conflicts are resolved with complete accuracy. The first assumption is only justified as a first approximation. This, and the fact that the measurers rejected $\sim$ 18% of the scanned events as being improperly classified, indicates that the 70% to 75% figure significantly overestimates the scanning efficiency. Note, however, that the average of $\sim$ 350 2γ events per roll is consistent with the number found by physicists.

The mass spectrometer results were used to obtain an independent estimate of the scanning efficiency. Let N_{spec} be the number of ω

events obtained from the mass spectrum of all 2π-trigger events, let $N_{2\gamma}$ be the corresponding number from the selected 2γ sample and let $\langle f_{2\gamma} \rangle$ be the fraction of ω events having both γ's from the π^o decay in the spark chambers as determined by the Monte Carlo calculation. Then from

$$N_{2\gamma}/(N_{spec} \langle f_{2\gamma} \rangle) \qquad (A.1)$$

we find a scanning efficiency of (41 ± 9)%.

There are two difficulties in determining the proper background subtraction for the 2π-trigger spectra. These are due to a possible $\rho(765)$ signal and the non-uniform mass acceptances of the spectrometer. Our limited statistics and lack of knowledge of the detailed nature of the background preclude a quantitative analysis of these effects. Their qualitative effect would be to yield an anomalously low background and over estimate the ω signal. As a consequence, we feel the figure of 41% is probably somewhat low.

APPENDIX B

COMMENT ON THE πN CHARGE EXCHANGE CROSS SECTIONS

To check the efficiency of the neutron counters used in this experiment, the differential cross section data of Chiu, et al.[21] at 1.44 GeV/c (T_π = 1.3 GeV) for the reaction $\pi^- p \rightarrow \pi^o n$ was selected as a standard. In Figure B.1 we show the efficiencies obtained from our charge exchange data based on the data of Chiu, et al. Data on η^o production was also obtained from that experiment (Richards, et al.[30]) and four points based on these data are also plotted.

The disturbing feature of these data is the deep dip centered on a neutron kinetic energy of 200 MeV. The agreement between the π^o and η^o points, which correspond to different counters, implies that dip is a real feature of the data and not due to problems with one or two counters.

In an attempt to understand the possible causes of this dip, we undertook to compare Chiu's data with other experiments at comparable energies. The data from Chiu, et al. and from Bulos, et al.[31] at p = 1.25 GeV/c are shown in Figure B.2. Chiu's data points include both the statistical error and normalization uncertainty. The errors on Bulos' results are comparable. Figure B.3 shows Chiu's data at 1.43 GeV/c and data from Crouch, et al.[22] at 1.395 and 1.469 GeV/c. We estimate 10% errors on Crouch's data and have indicated a typical error bar. The counter efficiencies calculated from Crouch's data are shown in Figure IV.10.

Figure B.4 shows the differential cross section calculated from our data using the neutron counter efficiency function calculated by Kurz's program for a 6 MeV threshold (Figure IV.10).

The essential features of Figure IV.10 may now be easily related to the cross section data. The two high points at T_n = 54 and 82 MeV

Figure B.1. Neutron counter efficiencies based on the data of Chiu, et al. The curve represents the results of Kurz's program for a 6 MeV threshold.

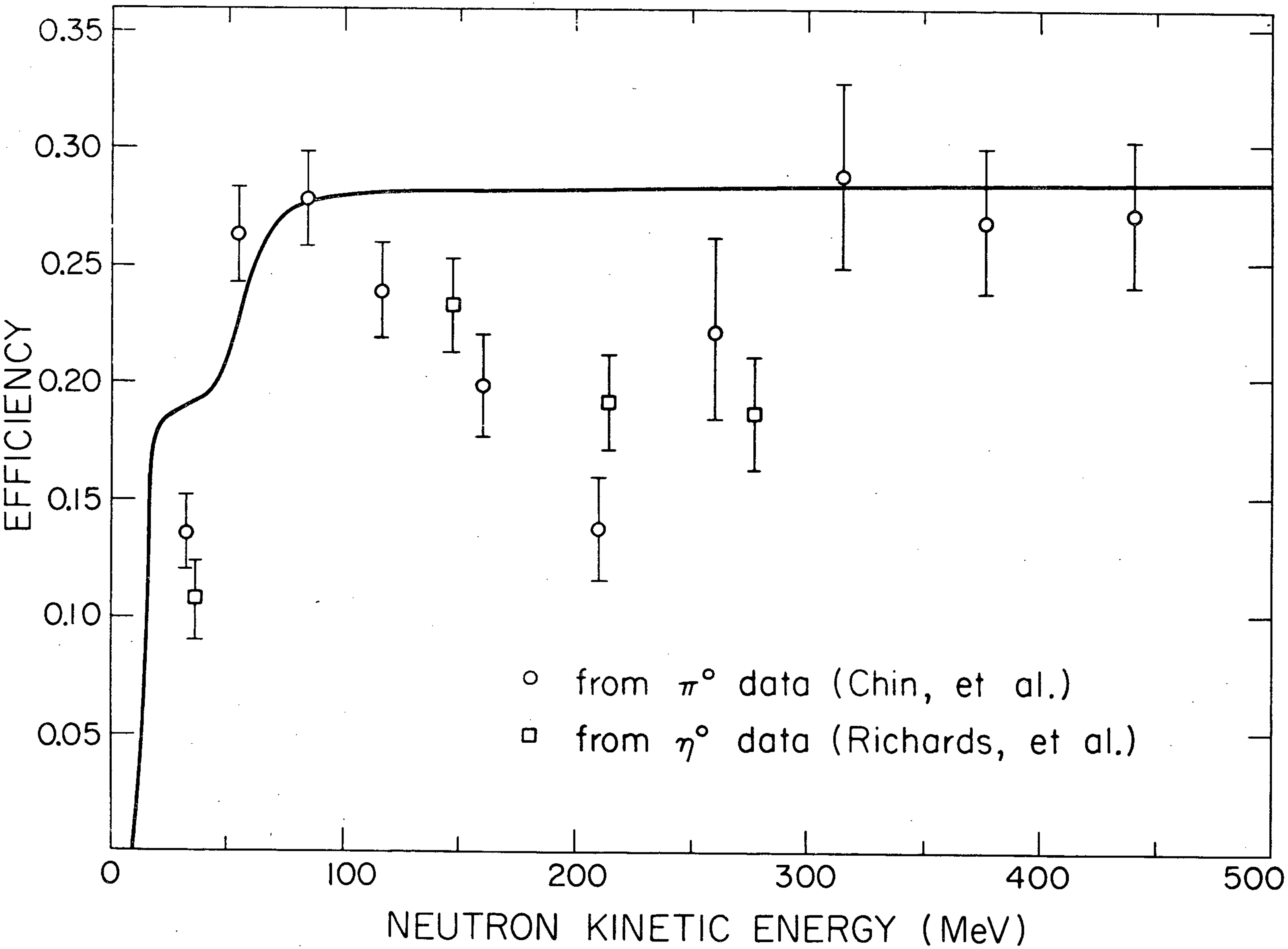
0.35
0.30
0.25
0.20
0.15
0.10
0.05
EFFICIENCY
0
100
200
300
400
500
NEUTRON KINETIC ENERGY (MeV)
○ from π° data (Chin, et al.)
□ from η° data (Richards, et al.)

Figure B.2. Comparison of the data from Chiu, et al. and Bulos, et al. on $\pi^- p \to \pi^0 n$ at $p_\pi = 1.25$ GeV/c

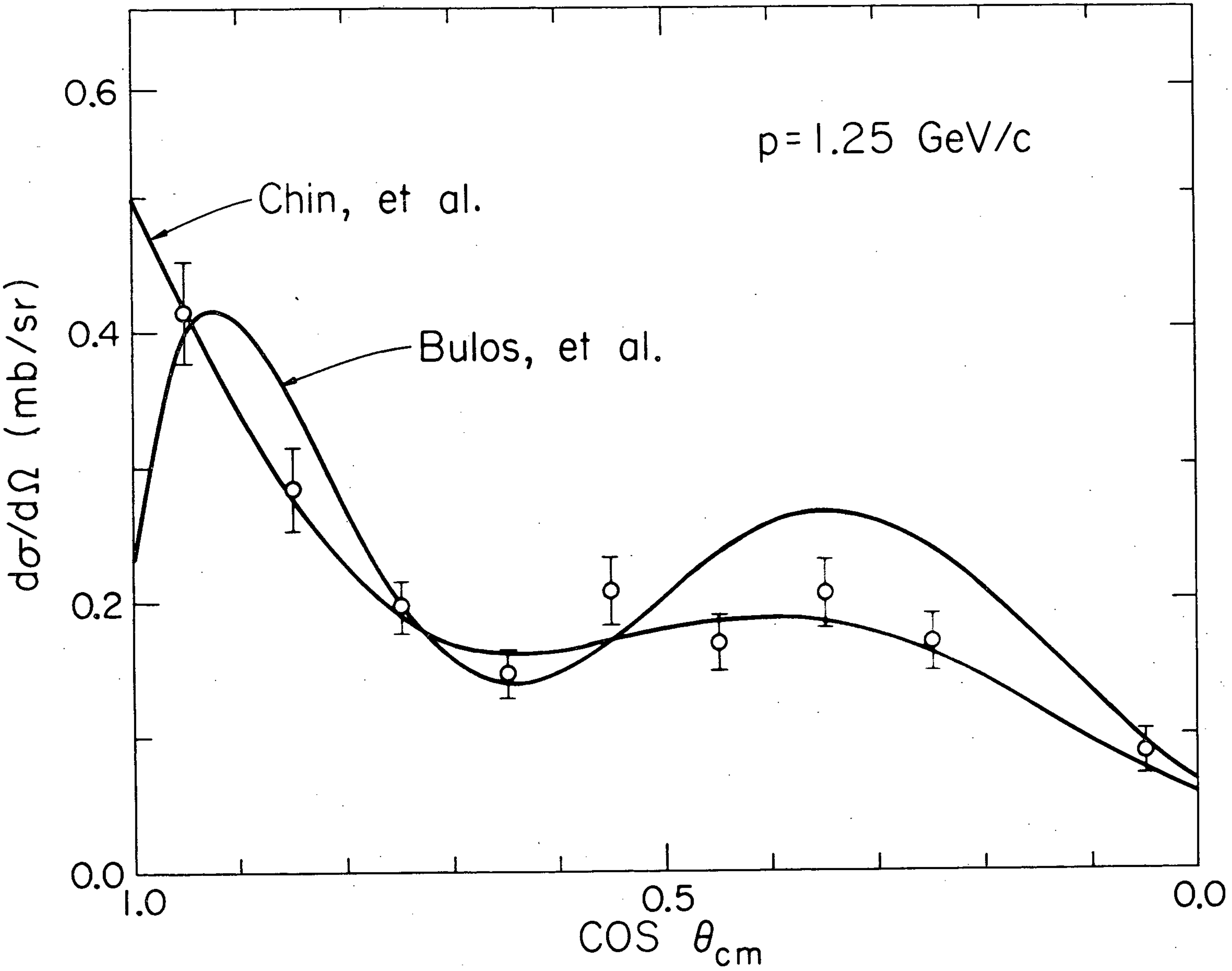
p=1.25 GeV/c
Chin, et al.
Bulos, et al.
dσ/dΩ (mb/sr)
0.6
0.4
0.2
0.0
1.0
0.5
0.0
COS θcm

Figure B.3. Comparison of the data from Chiu, et al. at $p_\pi = 1.43$ GeV/c and Crouch, et al. at 1.395 and 1.469 GeV/c.

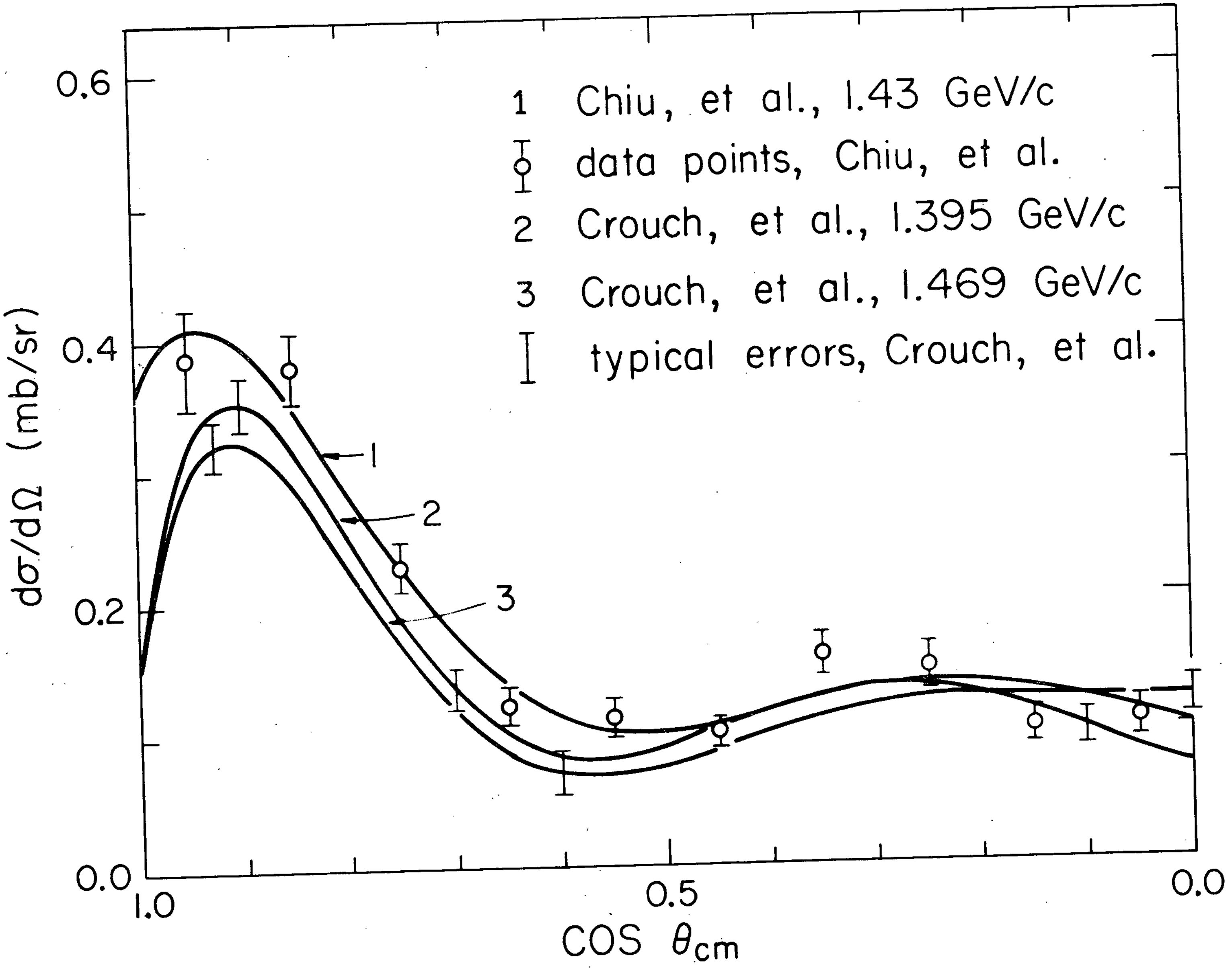

1 Chiu, et al., 1.43 GeV/c
data points, Chiu, et al.
2 Crouch, et al., 1.395 GeV/c
3 Crouch, et al., 1.469 GeV/c
typical errors, Crouch, et al.
1
2
3
dσ/dΩ (mb/sr)
0.6
0.4
0.2
0.0
1.0
0.5
0.0
COS θcm

Figure B.4. Differential cross section from our data on $\pi^- p \rightarrow \pi^o n$ at p_π = 1.44 GeV/c based on the calcuated neutron counter efficiency.

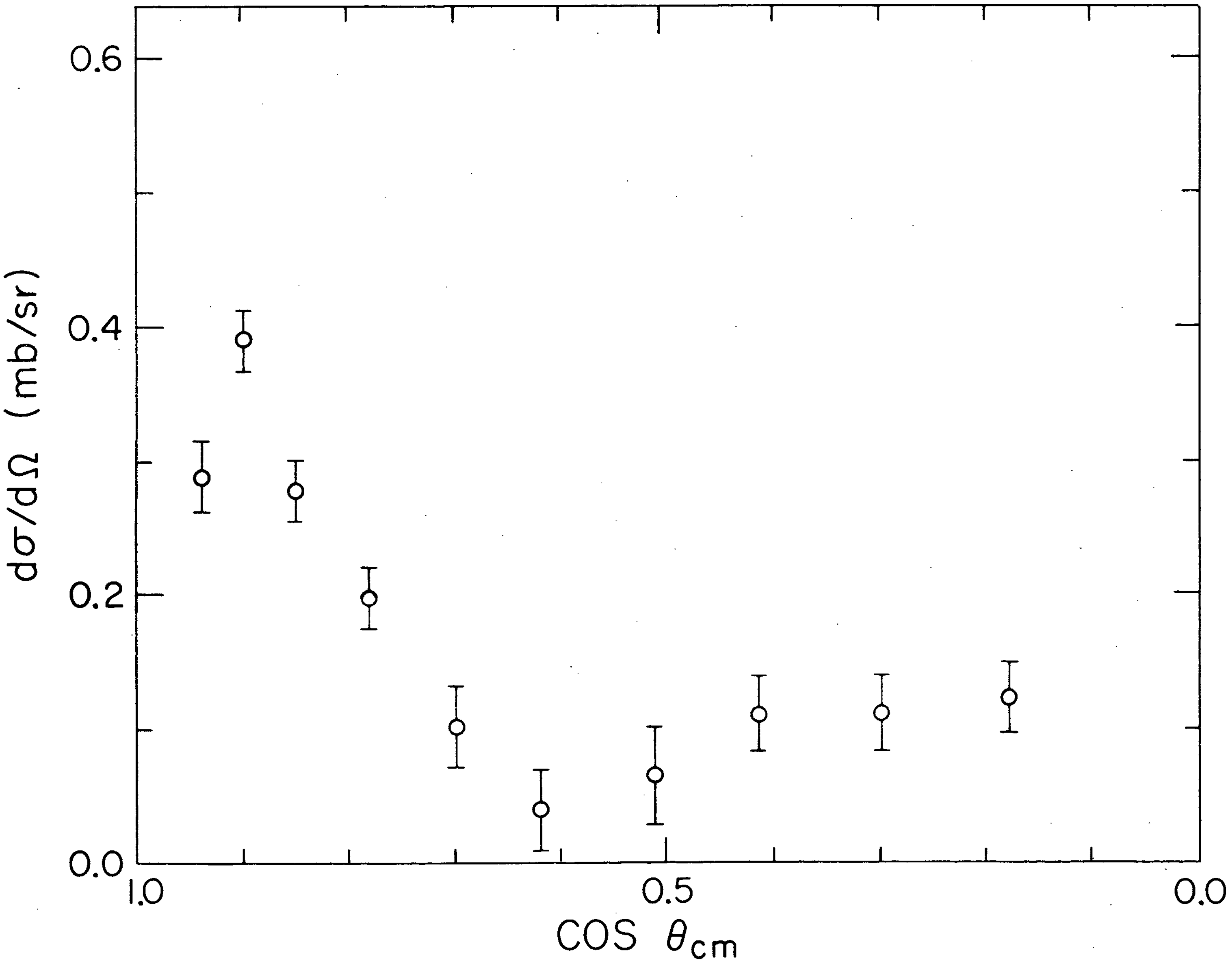
0.6
0.4
0.2
0.0
dσ/dΩ (mb/sr)
1.0
0.5
0.0
COS θ_{cm}

correspond to the first maximum in the charge exchange differential cross section and thus are most sensitive to the normalization uncertainty. The low point at T_n = 210 MeV corresponds to the region around the first minimum in the differential cross section and is sensitive both to its precise position and the slope of the forward peak.

Perhaps the most important consequence of these observations is that rather smaller slope of the forward peak seen in Chiu's data would underestimate the contribution of higher partial waves in πN phase shift analysis. Our data do not allow a definite statement on this point but do raise questions about the existing data.

From the general agreement (except at the above mentioned dip) between our measured neutron counter efficiencies and the calculated efficiencies we conclude that the results of Kurz's program are essentially correct. We subsequently use the calculated neutron counter efficiencies.

LIST OF REFERENCES

1. Particle Data Group, Phys. Letters 33B, 1 (1970).

2. K. Gottfried, J. D. Jackson, Nuovo Cimento 33, 309 (1964).

3. J. P. Ader, M. Capdeville, G. Cohen-Tannoudji, Ph. Salin, Nuovo Cimento 61A, 952 (1968).

4. J. D. Jackson, Rev. Mod. Phys. 37, 484 (1965).

5. J. D. Jackson, J. T. Donahue, K. Gottfried, R. Keyser, B. E. Y. Svensson, Phys. Rev. 139, B428 (1965).

6. V. D. Barger, D. B. Cline, Phenomenological Theories of High Energy Scattering (W. A. Benjamin, Inc., New York, 1969).

7. L.-L. Wang, Phys. Rev. Letters 16, 756 (1966).

8. M. Jacob, G. C. Wick, Ann. Phys. (N.Y.) 7, 404 (1959).

9. M. Barmawi, Phys. Rev. Letters 16, 595 (1966).

10. G. E. Hite, Ph. D. Thesis, University of Illinois, 1967.

11. M. Nobuyama, Prog. Theor. Phys. 41, 730 (1969).

12. E. I. Rosenberg, Ph. D. Thesis, University of Illinois, 1971.

13. C. E. Wiegand, T. Elioff, W. B. Johnson, L. B. Auerbach, J. Lach, T. Ypsilantis, Rev. Sci. Instr. 33, 526 (1962).

14. G. Galti, P. Hillman, W. C. Middelkoop, T. Yamagata, E. Zavattini, Nucl. Instr. and Meth. 29, 77 (1964).

15. D. G. Crabb, J. G. McEwen, E. G. Auld, A. Langsford, Nucl. Instr. and Meth. 48, 87 (1967).

16. C. Geweniger, Diplomarbeit, Universität Hamburg, 1967.

17. D. Bollini, A. Buhler-Broglin, P. Dalpiaz, T. Massam, F. Navach, F. L. Navarria, M. A. Schneegans, F. Zetti, A. Zichichi, Nuovo Cimento 61A, 125 (1969).

18. J. B. Hunt, C. A. Baker, C. J. Batty, P. Ford, E. Friedman, L. G. Williams, Nucl. Instr. and Meth. 85, 269 (1970).

19. R. J. Kurz, unpublished report, UCRL-11339 (1964).

20. T. J. Gooding, H. G. Pugh, Nucl. Instr. and Meth. 7, 189 (1960).

21. C. B. Chiu, R. D. Eandi, A. C. Helmholz, R. W. Kenny, B. J. Moyer, J. A. Poirier, W. B. Richards, R. J. Cence, V. Z. Peterson, N. K. Sehgal, V. J. Stenger, Phys. Rev. 156, 1415 (1967).

22. H. R. Crouch, Jr., R. Hargraves, R. E. Lanou, Jr., J. T. Massimo, A. E. Pifer, A. M. Shapiro, M. Wigdoff, A. E. Brenner, M. Ioffredo, F. D. Rudnick, G. Cavelli, F. Gasparini, L. Guerriero, G. A. Salandin, A. Tomasin, C. Voci, F. Waldner, Y. Eisenberg, E. E. Ronat, S. Toaff, P. Bastien, B. Brabson, B. T. Feld, V. Kistiakowsky, Y. Goldschmidt-Clermont, D. Miller, I. A. Pless, A. Rogers, L. Rosenson, L. Ventura, T. L. Watts, R. K. Yamamoto, Phys. Rev. Letters 21, 849 (1968).

23. T. C. Bacon, W. J. Fickinger, D. G. Hill, H. W. K. Hopkins, D. K. Robinson, E. O. Salant, Phys. Rev. 157, 1263 (1967).

24. R. J. Miller, S. Lichtman, R. B. Willmann, Phys. Rev. 178, 2061 (1969).

25. G. S. Abrams, B. Eisenstein, H. Gordon, Phys. Rev. Letters 23, 673 (1969).

26. N. Armenisi, B. Ghidini, V. Picciarelli, A. Romano, A. Silvestri, A. Forino, R. Gessaroli, L. Lendinaro, A. Quareni-Vignudelli, A. Cartacci, M. G. Dagliano, G. diCaporiacco, M. Barrier, D. Mettel, J. Quinguard, Nuovo Cimento 65A, 637 (1970).

27. M. S. Farber, J. V. DePinto, N. N. Biswas, N. M. Cason, B. J. Deery, V. P. Kenny, J. A. Poirier, O. R. Sander, W. D. Shephard, Nucl. Phys. B29, 237 (1971).

28. J. A. J. Matthews, J. D. Prentice, T. S. Yoon, J. T. Carroll, M. W. Firebaugh, W. D. Walker, Phys. Rev. Letters 26, 400 (1971).

29. D. M. Ritson, Techniques of High Energy Physics (Interscience Publishers, Inc., New York, 1961).

30. W. B. Richards, C. B. Chiu, R. D. Eandi, A. C. Helmholz, R. W. Kenny, B. J. Moyer, J. A. Poirier, R. J. Cence, V. Z. Peterson, N. K. Sehgal, V. J. Stenger, Phys. Rev. D 1, 10 (1970).

31. F. Bulos, R. E. Lanou, A. E. Pifer, A. M. Shapiro, C. A. Bordner, A. E. Brenner, M. E. Law, E. E. Ronat, F. D. Rudnick, P. Bastien, B. B. Brabson, Y. Eisenberg, B. T. Feld, V. K. Kistiakowsky, I. A. Pless, L. Rosenson, R. K. Yamamoto, G. Cavelli, F. Gasparini, L. Guerriero, G. A. Salandin, A. Tomasin, L. Ventura, C. Voci, F. Waldner, Phys. Rev. 187, 1827 (1969).

VITA

Allison Dean Russell was [redacted] on [redacted] He attended public school there and graduated from Saint John High School in June, 1960. He entered the Massachusetts Institute of Technology in September, 1960, and received the Bachelor of Science degree in physics in June, 1964.

He entered the Graduate College of the University of Illinois in September, 1964, and received the Master of Science degree in February, 1966. He held a combination of teaching and research assistantships during his graduate studies. He is co-author of the paper "A Measurement of the Ratio of the τ' Partial Decay Rates: $\Gamma(K^- \to \pi^-\pi^0\pi^0)/\Gamma(K^+ \to \pi^+\pi^0\pi^0)$", Phys. Rev. 186, 1403 (1969).